J. Fluid Mech. (2023), *vol*. 968, A11, doi:10.1017/jfm.2023.516

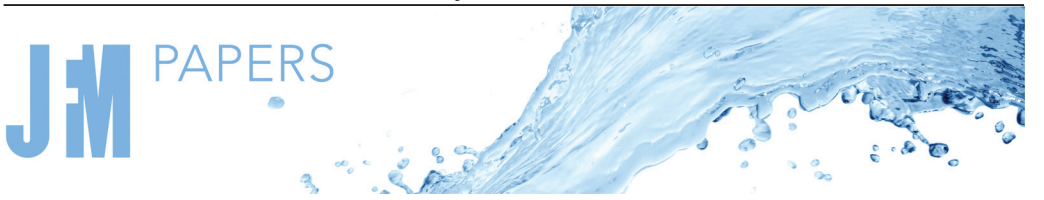

Separate and joint clustering characteristics of large-Stokes-number sprays subjected to turbulent co-flows

Ali Rostami[1], **Ri Li**[1] **and Sina Kheirkhah**[1],†

[1]School of Engineering, University of British Columbia, Kelowna, BC, Canada V1V1V7

(Received 26 December 2022; revised 11 June 2023; accepted 18 June 2023)

Separate and joint droplets, clusters, and voids characteristics of sprays injected in a turbulent co-flow are investigated experimentally. Simultaneous Mie scattering and interferometric laser imaging for droplet sizing along with separate hotwire anemometry are performed. The turbulent co-flow characteristics are adjusted using zero, one or two perforated plates. The Taylor-length-scale-based Reynolds number varies from 10 to 38, and the Stokes number estimated based on the Kolmogorov time scale varies from 3 to 25. The results show that the mean length scale of the clusters normalized by the Kolmogorov length scale varies linearly with the Stokes number. However, the mean void length scale is of the order of the integral length scale. It is shown that the number density of the droplets inside the clusters is approximately 7 times larger than that in the voids. The ratios of the droplets number densities in the clusters and voids to the total number density are independent of the test conditions and equal 5.5 and 0.8, respectively. The joint probability density function of the droplets diameter and clusters area shows that the droplets with the most probable diameter are found in the majority of the clusters. It is argued that intensifying the turbulence broadens the range of turbulent eddy size in the co-flow which allows for accommodating droplets with a broad range of diameters in the clusters. The results are of significance for engineering applications that aim to modify the clustering characteristics of large-Stokes-number droplets sprayed into turbulent co-flows.

Key words: particle/fluid flow

1. Introduction

Turbulent particle-laden flows are of relevance to many engineering applications such as gas turbine engine combustors used for aircraft propulsion, cyclones used for particle separation, industrial driers and slurry pumps, see the works of Crowe *et al.* (2011),

† Email address for correspondence: sina.kheirkhah@ubc.ca

Kuerten (2016) and Zhao *et al.* (2021). Thus, several theoretical, numerical and experimental investigations have been carried out over the past decades, and many review papers have been published, see for example those of Poelma & Ooms (2006), Balachandar & Eaton (2010) and Brandt & Coletti (2022). Review of these studies suggests that, among many non-dimensional parameters, the Stokes number (which is the ratio of particle to flow time scale, as defined by, for example, Crowe *et al.* 2011) primarily influences the characteristics of the turbulent particle-laden flows. Although past investigations are of significant importance as they provide insight into relatively small and moderate Stokes number flows ($St \lesssim 10$), the Stokes number of particle-laden flows relevant to some engineering applications such as sprays in gas turbine engine combustors, is relatively large ($St \gtrsim 10$). The present study is motivated by the need for understanding the spray characteristics at relatively large Stokes numbers. As elaborated by Baker *et al.* (2017) and Boddapati, Manish & Sahu (2020), the interaction of the particles and the background turbulent flow leads to the formation of regions with relatively large and small number of particles, which are referred to as clusters and voids, respectively, and are relevant to the present study. A brief review of the literature related to the clusters and voids is provided below.

The inertial bias and sweep-stick mechanisms are proposed in the literature to elaborate the formation of clusters and voids in turbulent flows. The former suggests that during a particle and eddy interaction, the large eddies centrifuge out the particles and accumulate them in regions that feature small vorticities and large strain rates, as explained by Maxey (1987), Squires & Eaton (1991) and Wang & Maxey (1993). Compared with the inertial bias mechanism, the sweep-stick mechanism suggests that the vorticity and strain rate fields may not be sufficient in explaining the positioning of the particles and hence formation of the clusters, see the work of Goto & Vassilicos (2008). The sweep-stick mechanism suggests that particles with $St \gtrsim 1$ tend to be positioned in the spatial locations with zero acceleration. Then, these particles are carried by large eddies in the flow, see the works of Goto & Vassilicos (2006), Monchaux, Bourgoin & Cartellier (2012), Mora *et al.* (2021) and Hassaini & Coletti (2022).

Various tools and methods have been developed to identify the clusters and voids from the spatial distribution of the particles. For example, Monchaux, Bourgoin & Cartellier (2010), Tagawa *et al.* (2012) and Frankel *et al.* (2016) utilized the Voronoï cells, Andrade, Hardalupas & Charalampous (2022) used the combined graph and Voronoï cells, Fessler, Kulick & Eaton (1994) and Villafañe-Roca *et al.* (2016) implemented the box-counting method, and Salazar *et al.* (2008), Saw *et al.* (2008) and Sahu, Hardalupas & Taylor (2016) applied the radial distribution functions to identify the clusters. The Voronoï cells (relevant to the present investigation) can allow for estimating the degree of clustering, which is defined (see for example Boddapati *et al.* 2020) as the root mean square (RMS) of the normalized Voronoï cells area (σ) divided by that if the droplets were distributed following a random Poisson process (RPP), σ_{RPP}, minus unity. The studies of Monchaux *et al.* (2010), Obligado *et al.* (2014) and Sumbekova *et al.* (2017) showed that the degree of clustering is influenced by three non-dimensional parameters that are the Stokes number (St) estimated based on the Kolmogorov time scale, Taylor-length-scale-based Reynolds number (Re_λ) and the droplets volume fraction (ϕ_{v}). Monchaux *et al.* (2010) and Obligado *et al.* (2014) showed that for relatively small values of the Stokes number ($St \lesssim 10$) and for relatively small values of the Taylor-length-scale-based Reynolds number ($Re_\lambda \lesssim 200$), the degree of clustering increases by increasing the Stokes number and maximizes at $St \approx 2$–4. Further increasing the Stokes number decreases the degree of clustering. Compared with those of Monchaux *et al.* (2010) and Obligado *et al.* (2014), the study of

Sumbekova *et al.* (2017) showed that, for relatively small values of the Stokes number but relatively large values of the Taylor-length-scale-based Reynolds number ($Re_\lambda \gtrsim 200$), St does not greatly influence the degree of clustering, however, this parameter scales with Re_λ and the square root of ϕ_v. The studies of Sumbekova *et al.* (2017), Obligado *et al.* (2014) and Monchaux *et al.* (2010) showed that the probability density function (PDF) of the cluster and void areas feature power-law correlations with the exponents of the power-law ranging from approximately -1.5 to -2.1 and -1.7 to -1.9, respectively. Sumbekova *et al.* (2017) showed that the PDFs of the cluster and void areas normalized by their corresponding mean value feature a power-law decay with an exponent of $-5/3$ for normalized cluster and void areas ranging from approximately 0.2 to 10.

In addition to the PDFs of the cluster and void areas, the length scales of the clusters and voids and how they relate the length scales of the turbulent flow have been studied. The characteristic length scales of the clusters and voids are defined as the square root of the cluster and void mean areas, respectively. The studies of Aliseda *et al.* (2002), Obligado *et al.* (2014), Sumbekova *et al.* (2017), Sahu *et al.* (2016) and Boddapati *et al.* (2020) showed that the cluster length scale is approximately 5–90 times the Kolmogorov length scale. For voids, Sumbekova *et al.* (2017) showed that the length scale can increase to approximately 200 times the Kolmogorov length scale. Power-law formulations were developed by Sumbekova *et al.* (2017) and it was shown that the normalized cluster length scale is proportional to $St^{-0.25}Re_\lambda^{4.7}\phi_v^{1.2}$. Also, Sumbekova *et al.* (2017) showed that, despite the Stokes number does not significantly influence the normalized voids length scale, this positively relates to Re_λ and ϕ_v.

Although the generated knowledge from the particle-laden flow studies (with a brief review presented above) is of significant importance, as it allows to understand the clustering characteristics of droplets corresponding to relatively small Stokes numbers ($St < 10$), some engineering application feature droplets with large Stokes numbers. In such applications, it is of significant importance to understand the distribution of the droplet diameter and their number density within a given cluster and for $St > 10$. For example, for spray combustion-related applications (which feature Stokes numbers in excess of 10), the mean distance between the fuel droplets and their number density within a given cluster can influence the droplet evaporation rate as well as the flame location and the temperature distribution, see for example the works of Sahu, Hardalupas & Taylor (2018), Hardalupas, Taylor & Whitelaw (1994), Akamatsu *et al.* (1996), Pandurangan & Sahu (2022) and Weiss *et al.* (2021). The objective of the present study is to investigate the effect of the Stokes number on both the geometrical (e.g. clusters and voids length scales) as well as the joint characteristics of the droplets and clusters/voids for $St > 10$. In the following, the methodology, data reduction, results and concluding remarks are presented in §§ 2–5, respectively.

2. Experimental methodology

The experimental set-up, the utilized diagnostics and the tested conditions are presented in this section.

2.1. *Experimental set-up*

The experimental set-up consists of a liquid delivery and flow apparatuses, which are shown in figure 1 as items (1–3) and item (4), respectively. A nitrogen bottle, item (1) in the figure, as well as a dual-valve MCRH 2000 ALICAT pressure controller, item (2), were used to purge water inside a pressure vessel, item (3). Then, water flowed into the

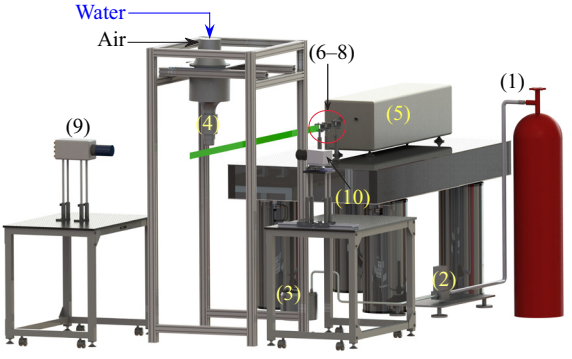

Figure 1. Experimental set-up. Items (1–3) are a nitrogen bottle, a pressure controller and a pressurized water vessel. Item (4) is the nozzle section of the flow apparatus. Item (5) is a 532 nm Nd:YAG laser. Items (6–8) are the laser sheet forming optics and optomechanics. Items (9) and (10) are a Nova S12 camera and lens as well as a Zyla camera and lens for simultaneous Mie scattering and interferometric laser imaging for droplet sizing (ILIDS) measurements.

flow apparatus, see the blue arrow in figure 1. In addition to water, a compressor was used to provide air into the flow apparatus, see the black arrow in figure 1. The air flow rate was controlled using an MCRH 5000 ALICAT mass flow controller.

The flow apparatus is composed of a diffuser section (with an area ratio of 4), a settling chamber (which is equipped with five equally spaced mesh screens), a contraction section (with an area ratio of 7) and a nozzle (with an inner diameter of 48.4 mm). Further details regarding the apparatus are provided by Mohammadnejad, Saca & Kheirkhah (2022), Kheirkhah & Gülder (2015) and Kheirkhah (2016). The nozzle section of the flow apparatus is shown in figure 2. In the present study, this section was modified to allow for producing a spray subjected to turbulent co-flow of air. The nozzle includes a 6.4 mm outer diameter tube (which carries water), a spray injector, a turbulence generation mechanism and a ring-shaped tube-holder, which was press-fit against the inner wall of the nozzle and the outer wall of the tube using four bars and a collar. The injector was a pressure swirl atomizer from Delavan (model 6330609), which produced a polydisperse spray. The spray flow rate depends on the vessel pressure, and separate calibration experiments were performed to obtain the relation between the vessel pressure and the spray flow rate, as discussed in Appendix A.

Three turbulence generation mechanisms were used in the present study. Either no perforated plate, one perforate plate (see figure 2*a*) or two perforated plates attached back-to-back (see figure 2*b*) were utilized. The outer diameter of each perforated plates is 48.4 mm, matching the inner diameter of the nozzle. Each perforated plate features 3.9 mm diameter holes arranged in a hexagonal pattern. For the first turbulence generation mechanism, the perforated plates in figure 2 were removed. For the third turbulence generation mechanism, the plates were rotated by 60° with respect to one another, similar to that in the study of Kheirkhah & Gülder (2014). For the second turbulence generation mechanism, the planes containing the holes, and for the third turbulence generation mechanism, the centre plane of the two perforated plates, were positioned 76.0 mm upstream of the nozzle exit plane, similar to the studies of Kheirkhah & Gülder (2015) and Kheirkhah (2016).

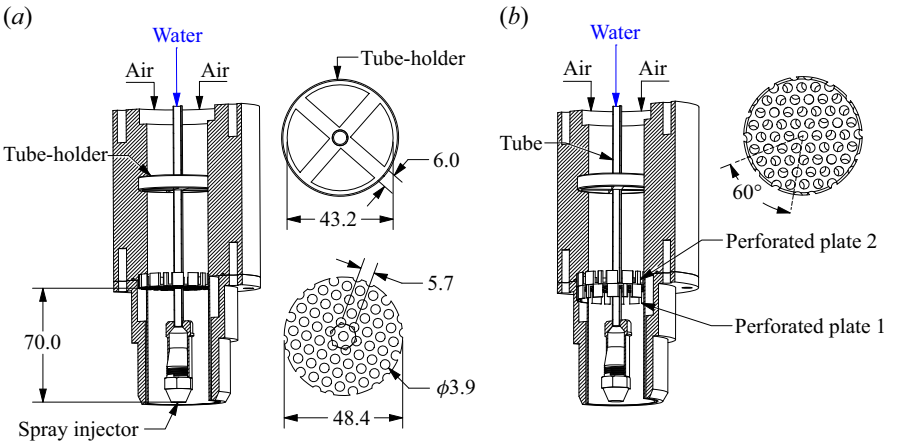

Figure 2. (*a*) and (*b*) Three-dimensional (3-D) drawing of the flow apparatus nozzle section for the second and third turbulence generation mechanisms, respectively.

2.2. *Diagnostics*

Separate hotwire anemometry (HWA) as well as simultaneous Mie scattering and interferometric laser imaging for droplet sizing (ILIDS) were performed. The hotwire anemometry was used to characterize the background turbulent flow. A schematic of the diagnostics used in the present study is shown in figure 1. The hardware configuration for the HWA is identical to that used by Mohammadnejad *et al.* (2022); so a separate illustration is not presented in figure 1. For all test conditions, the HWA data were acquired at a frequency of 100 kHz and for 90 s, corresponding to 9 000 000 data points. The simultaneous Mie scattering and ILIDS images were collected at a frequency of 10 Hz and for a duration of 80 s, corresponding to 800 image pairs. Further details regarding the HWA, Mie scattering and ILIDS diagnostics are provided in the following.

2.2.1. *Hotwire anemometry*

The hardware of the HWA system consists of a probe (model 55P01 from Dantec), a probe support (model 9055H0261 from Dantec) and two motorized translational stages (MTS50-Z8 from Thorlabs). The probe is a single wire sensor, which is 3 mm long (with an active sensor length of 1.25 mm) and has a diameter of 5 μm. A mini-constant temperature anemometry (mini-CTA) circuit (model 9054T0421 from Dantec) maintains the wire temperature, with an overheat ratio of 0.7. The motorized translational stages featured a 50 mm range of operation, which was sufficient for the present study. Further details regarding the HWA system as well as the calibration procedure are provided by Mohammadnejad *et al.* (2022).

A Cartesian coordinate system was used in the present investigation. The origin of the coordinate system is at the exit plane of the nozzle section and at the nozzle centreline, as shown in figure 3. The z-axis coincides with the nozzle centreline. The x-axis is normal to the z-axis and is parallel with the laser sheet shown in figure 1. HWA was performed at $z = 35.0$ mm and at horizontal locations spaced by 5.0 mm along the x-axis, ranging from $x = -20.0$ to 20.0 mm as shown by the red cross data symbols in figure 3.

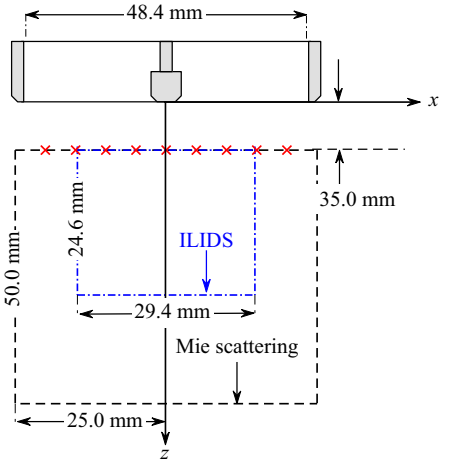

Figure 3. Coordinate system and the measurements locations. The red cross data points present the locations at which the hotwire anemometry was performed. The dashed black and dash–dotted blue squares are the regions of interest for the Mie scattering and ILIDS measurements, respectively. The minimum vertical distance for the above measurements is 35.0 mm from the nozzle exit plane, and this distance shown in the figure is not to scale.

2.2.2. *Mie scattering*

The Mie scattering hardware consists of a pulsed Nd:YAG laser (Lab-Series-170 from Spectra Physics, shown by item (5) in figure 1), the sheet forming optics (see items (6–8)) and a camera equipped with collection optics (item (9)). The laser produces a 1064 nm beam, which is converted to a 532 nm beam using a harmonic generator. The laser was operated at a reduced (compared to its maximum) but fixed energy to avoid saturation in the collected Mie scattering images. The laser beam was 8.0 mm in diameter, which was converted to a 40 mm high and 1 mm thick laser sheet using a plano-concave cylindrical lens with a focal length of -100 mm, a plano-convex cylindrical lens with a focal length of 500 mm and a cylindrical lens with a focal length of 1000 mm, see items (6–8) in figure 1. The centreline of the collimated laser sheet was positioned at $z = 55.0$ mm. The Mie scattering images were acquired using a Photron Fastcam Nova S12 camera equipped with a Macro Sigma lens, which had a focal length of $f = 105$ mm and its aperture size was set to $f/2.8$. A bandpass filter with a centre wavelength and full width at half maximum of 532 and 20 nm was mounted on the camera lens. By adjusting the working distance of the camera, a field of view of 70.0 mm along the x-axis and 70.0 mm along the z-axis was obtained, which corresponds to a pixel resolution of $70\,\text{mm}/1024\,\text{pixels} = 68\,\mu\text{m}\,\text{pixel}^{-1}$. For analysis and presentation purposes, the above field of view was cropped to a 50.0 mm $\times$ 50.0 mm square, which is shown by the black dashed box in figure 3. It is noted that since the above field of view is close to the injector, the air entrainment may occur and the background turbulent air flow may be anisotropic. A field of view that is located farther from the injector could facilitate reducing the effect of the air entrainment into the spray on the reported results and/or improve the background turbulent flow isotropy. However, the present study employed an injector that is used for reacting flow applications for which the majority of the turbulence and droplet interaction takes place close to the injector. In fact, at distances larger than 85 mm and for reacting conditions (not discussed here), the droplets are evaporated, burned and do not exist. For this reason, a field of view that is close to the injector is chosen. At distances smaller than

35 mm, the spray was too dense and the images were influenced by the laser reflection from the injector; as a result, the analysis of the Mie scattering images was not feasible.

2.2.3. *Interferometric laser imaging for droplet sizing*

ILIDS was performed to measure the droplets diameter, similar to that done by Qieni *et al.* (2016), Bocanegra Evans *et al.* (2015) and Garcia-Magarino *et al.* (2021). In ILIDS, the droplet diameter is measured by analysing the interference pattern of the reflected and first-order refracted rays scattered from spherical droplets that are illuminated by a laser. The ILIDS hardware includes the laser and the laser-sheet forming optics, see items (5–8) in figure 1, which are identical to those used for the Mie scattering technique as well as a scientific complementary metal-oxide semiconductor (sCMOS) camera equipped with a Macro sigma lens ($f = 105$ mm and aperture size of $f/2.8$) and a high-precision rotary stage, see item (10). The camera is a 5.5 Zyla from Andor, which has a 2560 pixels $\times$ 2160 pixels sensor. The ILIDS field of view was 29.4 mm along the x-axis and 24.6 mm along the z-axis, which led to a pixel resolution of 29.4 mm/2560 pixels $=$ 11.4 μm pixel^{-1}. Using the rotary stage, the angle between the axis normal to the camera sensor and the direction of the laser sheet, θ, was adjusted. Sahu (2011) utilized the Mie scattering theory and obtained the variations of the intensities of the first-order refraction and reflected light versus the scattering angle for water droplets. For these droplets, they showed that the above intensities are equal at approximately $\theta = 69^\circ$, creating interference patterns with a maximized amplitude which leads to the best clarity of the fringe patterns. In the present study, and similar to those performed by Sahu (2011) and Sahu *et al.* (2016), θ was set to 69°. Finally, the formulation by Hayashi, Ichiyanagi & Hishida (2012) and Thimothée *et al.* (2016) was used to estimate the droplet diameter, which is given by

$$d = \frac{2\lambda_L N}{\alpha}\left[\cos\left(\frac{\theta}{2}\right) + \frac{m\sin\left(\frac{\theta}{2}\right)}{\sqrt{m^2 - 2m\cos\left(\frac{\theta}{2}\right) + 1}}\right]^{-1}, \tag{2.1}$$

where λ_L is the wavelength of the laser and is 532 nm. In (2.1), m is the droplets index of refraction, which equals 1.33 for water, and α is the collection angle of the scattered light. The collection angle depends on the utilized lens diameter (d_l, which is 60 mm), and the distance between the camera lens and the projected location of the droplets in the measurement plane (c). Specifically, the collection angle is calculated using $\alpha = 2\arctan[d_l/(2c)]$. In the present study, while d_l is fixed, c can vary from 195 to 205 mm. Thus, the collection angle is not constant across the image plane. Here, a fixed value of $c = 200$ mm was used which can lead to an error in the calculation of the droplet diameter. This error was quantified, and it was obtained that the maximum error due to the variation of c is less than 2.5 %.

In (2.1), N is the number of the fringes and is estimated using the procedure discussed in the next section. Substituting $N = 1$ and the values of λ_L, m, θ and α in (2.1), the droplet diameter per fringe is obtained, which is 1.97 μm. Since at least two fringes are required for the detection of the droplets, the minimum measurable diameter of the droplets is twice the diameter per fringe which is $2 \times 1.97\ \mu\text{m} \approx 4\ \mu\text{m}$. Also, considering the widths of the fringes, the maximum resolvable diameter is estimated and equals 150 μm. Challenges exist in performing simultaneous ILIDS and Mie scattering measurements as well as interpreting the results, which need to be addressed. Since the viewing angle of the ILIDS

TG	U (m s^{-1})	Re_D	u_0' (m s^{-1})	Λ (mm)	λ (mm)	η (μm)	d^* (μm)	Re_λ	St	ϕ_v ($\times 10^6$)
N.A.	0.0	N.A.	N.A.	N.A.	N.A.	N.A.	34	N.A.	N.A.	1.8
0PP	3.5	11 200	0.57	5.9	0.39	102	29	14.9	4.5	1.8
0PP	7.0	22 400	1.07	5.8	0.29	63	29	20.3	11.4	1.2
0PP	10.5	33 600	1.55	7.1	0.26	50	29	27.1	18.5	1.0
0PP	14	44 800	2.14	10.0	0.26	43	29	37.8	25.3	1.1
1PP	3.5	11 200	0.4	4.0	0.39	121	29	10.3	3.2	2.1
1PP	7.0	22 400	0.85	4.7	0.29	71	29	16.3	9.2	1.6
1PP	10.5	33 600	1.22	4.7	0.24	54	29	19.5	15.9	1.4
1PP	14.0	44 800	1.63	5.0	0.21	44	28	23.3	21.4	1.2
2PP	3.5	11 200	0.64	4.9	0.34	89	29	14.5	5.7	2.2
2PP	7.0	22 400	1.35	5.9	0.26	53	29	23.0	16.5	1.6
2PP	10.5	33 600	1.55	7.3	0.27	51	29	27.5	18.3	1.3
2PP	14.0	44 800	1.93	10.0	0.28	47	28	35.9	20.2	1.2

Table 1. Test conditions. TG stands for the turbulence generating mechanism. 0PP, 1PP and 2PP are the acronyms for zero, one and two perforated plates, respectively.

camera is different than that of the Mie scattering camera, simultaneous measurement of the location of the droplets using the Mie scattering and ILIDS techniques require registering the ILIDS images to the Mie scattering images. Even after the registration of the ILIDS image to the Mie scattering image, since the ILIDS images are out-of-focus, the centres of the droplets identified from the ILIDS images are not identical to those obtained form the Mie scattering images. Furthermore, due to the limitations of the ILIDS technique, the number of droplets detected in each frame of the ILIDS does not equate to that of the Mie scattering technique. The above potentially lead to uncertainty in estimating the joint characteristics of the droplets and clusters/voids. Details for addressing/assessing the issues related to the droplets centre discrepancy and average diameter uncertainty for the calculation of the joint characteristics are discussed in Appendices B and C, respectively.

2.3. *Test conditions*

In total, 13 experimental conditions were tested, with the corresponding details tabulated in table 1. The first row in the table highlights the test condition for which no co-flow is used and the spray is issued into the quiescent air. The first column in the table presents the utilized turbulence generation (TG) mechanism, with 0PP, 1PP and 2PP referring to zero, one and two perforated plates, respectively. For each turbulence generation mechanism, the mean bulk flow velocities of 3.5, 7.0, 10.5 and 14.0 m s^{-1} were tested. The bulk Reynolds number was calculated using $Re_D = UD/\nu$, with D being the nozzle diameter and ν being the air kinematic viscosity estimated at the laboratory temperature. The values of Re_D are tabulated in the third column of table 1. The RMS of the streamwise velocity (u_0') and the integral length scale (Λ) estimated at $x = 0$ and $z = 35.0$ mm are listed in the fourth and fifth columns of table 1, respectively. The integral length scale was calculated using the Taylor's frozen turbulence hypothesis, see the work of Taylor (1938), and following the procedure detailed by Mohammadnejad *et al.* (2022). Specifically, the integral length scale was calculated as the multiplication of the mean bulk flow velocity and the integral of the streamwise velocity auto-correlation from $t = 0$ to the first time that the auto-correlation

becomes zero. The Taylor (λ) and Kolmogorov (η) length scales were calculated using $\lambda = \Lambda(u_0'\Lambda/\nu)^{-0.5}$ and $\eta = \Lambda(u_0'\Lambda/\nu)^{-0.75}$. The values of λ and η are tabulated in the sixth and seventh columns of table 1. For all test conditions, the most probable droplet diameters (d^*) were obtained using the ILIDS diagnostic and are listed in the eighth column of the table. Further details regarding the size distribution of the droplets are discussed in § 4.1.

The Taylor-length-scale-based Reynolds number, the Stokes number and the liquid volume fraction are non-dimensional parameters that can potentially influence the interaction of the droplets with the background turbulent flow. The Taylor-length-scale-based Reynolds number was estimated using $Re_\lambda = u_0'\lambda/\nu$, with the corresponding values listed in the ninth column of table 1. In the present study, Re_λ varies from approximately 10 to 36, which corresponds to relatively small values. Following Reade & Collins (2000), the Stokes number was calculated using

$$St = \frac{1}{18}\frac{\rho_W}{\rho_A}\left(\frac{d}{\eta}\right)^2, \tag{2.2}$$

where ρ_W and ρ_A are the water and air densities, respectively, both estimated at the laboratory temperature. In (2.2), d is the droplet diameter. In the present study, d was selected as the most probable droplet diameter for estimation of the Stokes number, with the rationale for this selection discussed later. The values of St are tabulated in table 1 and range from approximately 3 to 25, which are relatively large compared to those of the studies that were performed in multi-phase wind tunnels. It is worth highlighting that, in addition to the most probable droplet diameter, the Sauter mean diameter was also estimated for all test conditions following the formulation given by Lefebvre & McDonell (2017). The Stokes number estimated based on the Sauter mean diameter and the Kolmogorov length scale varied from 17 to 150 and positively correlated with the Stokes number estimated based on the most probable droplet diameter and the Kolmogorov length scale. Additionally, instead of the Kolmogorov length scale, the Stokes number was also estimated based on the integral length scale. It was obtained that the Stokes numbers estimated based on both length scales positively correlate. Given the above correlations, presentation of the results using the Stokes number estimated based on either of the length scales or either of the diameters yielded similar conclusions. Nonetheless, facilitating comparisons with the past investigations, e.g. those of Sumbekova *et al.* (2017), Obligado *et al.* (2014) and Monchaux *et al.* (2010), the Stokes number estimated based on the most probable droplet diameter and the Kolmogorov length scale was used in the discussions and analyses.

Following the definition provided by Elghobashi (1994), the liquid volume fraction was calculated from

$$\phi_v = n\frac{V_d}{V_{ROI}}, \tag{2.3}$$

where n is the mean number of droplets within the volume of the region of interest (ROI), V_{ROI}. In (2.3), V_d is the droplet volume. For each test condition, n was estimated using the Mie scattering technique and averaged over all collected Mie scattering images. $V_{ROI} = 50\,\text{mm} \times 50\,\text{mm} \times 1\,\text{mm}$ and $V_d = (\pi/6)d^{*3}$. The values of ϕ_v are listed in the last column of table 1 and change from approximately 1×10^{-6} to 2×10^{-6}. Following Elghobashi (1994), the estimated liquid volume fractions are relatively small, rendering the tested sprays as dilute. In essence, compared to past studies, the non-dimensional parameters of the present study correspond to dilute sprays with small Taylor-length-scale-based Reynolds number but large Stokes numbers.

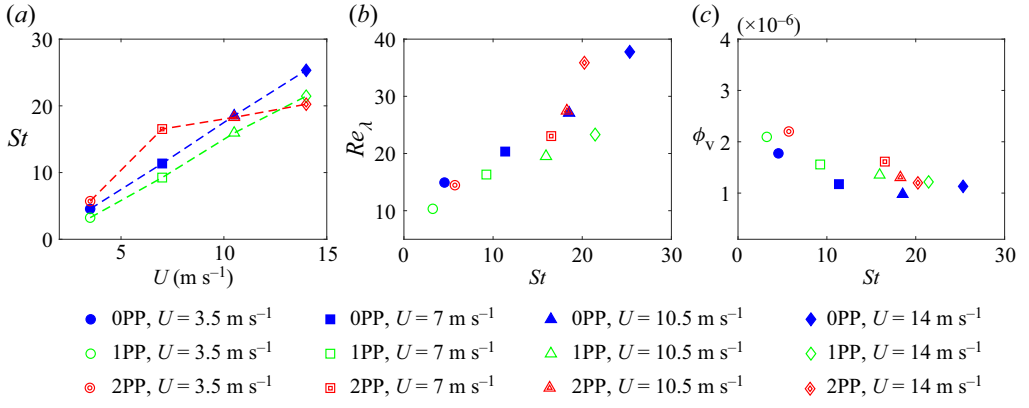

Figure 4. Variations of (*a*) the Stokes number versus mean bulk flow velocity, (*b*) the Taylor-length-scale-based Reynolds number versus Stokes number and (*c*) the liquid volume fraction versus the Stokes number. The blue, green and red colours correspond to turbulence generation mechanisms with zero, one and two perforated plates, respectively.

For all test conditions with the co-flow, St, Re_λ and ϕ_v vary by changing the mean bulk flow velocity and the turbulence generation mechanism. Variations of St versus U, Re_λ versus St and ϕ_v versus St are presented in figure 4(*a–c*), respectively. As can be seen, the variations of these non-dimensional parameters are mostly influenced by the mean bulk flow velocity. That is, increasing U increases St and Re_λ but decreases ϕ_v. It is important to note that, in the present study, changing the turbulence generation mechanism for a fixed value of U and changing U for a given turbulence generation mechanism both change the background RMS velocity fluctuations, which changes St, Re_λ and ϕ_v.

3. Data reduction

Of prime importance to the present study are identifications of clusters and voids as well as estimating the droplets diameter. The former and the latter are obtained using the Mie scattering and the ILIDS, respectively, with details provided in the following subsections.

3.1. *Clusters and voids identification*

The procedures followed to identify the clusters and voids are illustrated in figure 5. A representative raw Mie scattering image corresponding to the no co-flow test condition is shown in figure 5(*a*). The results in figure 5(*a*) were binarized to identify the centres of the droplets, which are shown by the black circular data points in figure 5(*b*). It is important to note that the laser intensity features a nearly top-hat profile in the region of interest. Also, the Mie scattering background field (averaged over 800 images taken with the camera lens capped) is approximately 0.2 % of the maximum acquired intensity. Thus, normalizing the Mie scattering images by the spatially varying laser intensity as well as subtracting the background field from the Mie scattering images did not influence the process for identifying the droplets centres in figure 5(*b*). Using the centres of the droplets along with the 'voronoi' function in MATLAB, the Voronoï cells around each droplet were obtained and overlaid on figure 5(*b*) using the black lines. As can be seen in figure 5(*b*), the area of the Voronoï cells located at the centre of the ROI is relatively small and increases towards the periphery of this region. Such increasing trend is related to the inhomogeneous seeding

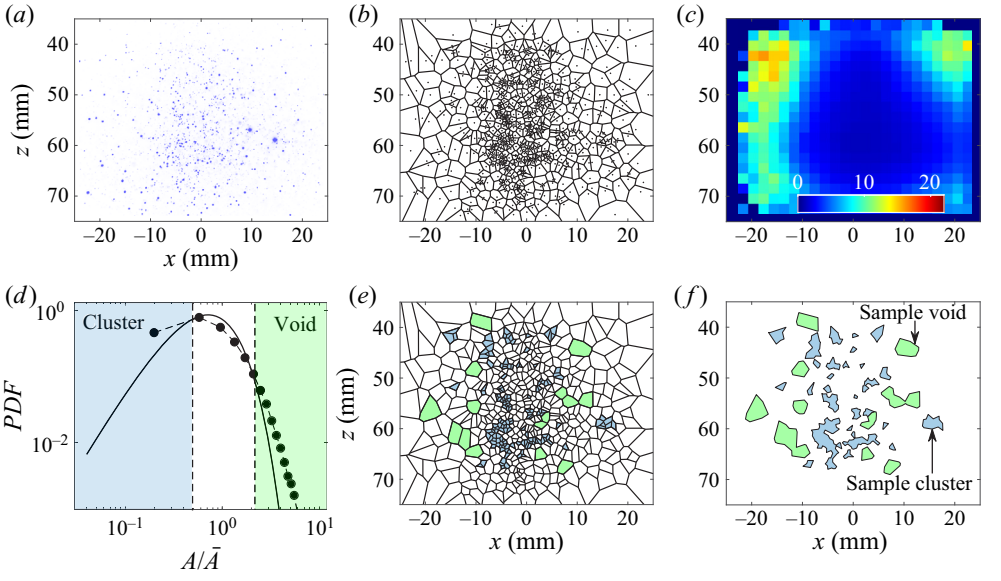

Figure 5. (*a*) Representative raw Mie scattering image corresponding to the no co-flow test condition. (*b*) Centres of the droplets in panel (*a*) and the Voronoï cells. (*c*) Spatial variation of the locally averaged Voronoï cells area. (*d*) PDF of the Voronoï cells areas normalized by their local mean. Overlaid in panel (*d*) is the PDF_{RPP} from (3.1). The dashed lines in panel (*d*) are $A/\bar{A} = 0.5$ and 2.2. (*e*) Cells with areas related to clusters (blue cells) and voids (green cells). (*f*) Clusters and voids corresponding to the Mie scattering image in panel (*a*).

of the droplets by the injector and can potentially lead to the incorrect identification of the clusters and voids which are formed because of the interaction of the droplets with the background turbulent flow. Aiming to address this issue, following Sumbekova *et al.* (2017), the values of the Voronoï cells area were normalized by the locally averaged value. Following this, first, the ROI was divided into several windows (widths and heights of Δx and Δz). Then, the areas of the Voronoï cells corresponding to the droplets within each of the above windows were obtained for all frames and were averaged, with the results shown in figure 5(*c*). The spatially varying $\bar{A}$, which is shown in figure 5(*c*), was used in the calculation of $PDF(A/\bar{A})$. In this calculation, all Mie scattering images were used, and the resultant PDF is presented in figure 5(*d*) with the black circular data points.

Provided the droplets spatial distribution followed the RPP, the PDF of $A/\bar{A}$, referred to as PDF_{RPP}, could be estimated using that of Ferenc & Néda (2007) which is given by

$$PDF_{\mathrm{RPP}} = \frac{b^a}{\Gamma(a)} \left(A/\bar{A}\right)^{a-1} \exp^{(-bA/\bar{A})}. \tag{3.1}$$

In (3.1), a and b are fitting parameters with $a = b = 3.5$, and Γ is the gamma function with $\Gamma(a) = 3.32$. The variation of PDF_{RPP} versus $A/\bar{A}$ was obtained and presented by the black solid curve in figure 5(*c*). Additionally, using MATLAB, 800 images were synthetically generated by distributing particles inside the domain of investigation randomly, with the number of droplets identical to that shown in figure 5(*a*), and the PDF of $A/\bar{A}$ was calculated. It was confirmed that the PDF of the Voronoï cells normalized area for randomly distributed particles closely follows the right-hand side of (3.1). Next, the intersections of PDF_{RPP} and the $PDF(A/\bar{A})$ for the results in figure 5(*d*) were obtained, which are shown by the dashed lines corresponding to $A/\bar{A} = 0.5$ and 2.2. The Voronoï

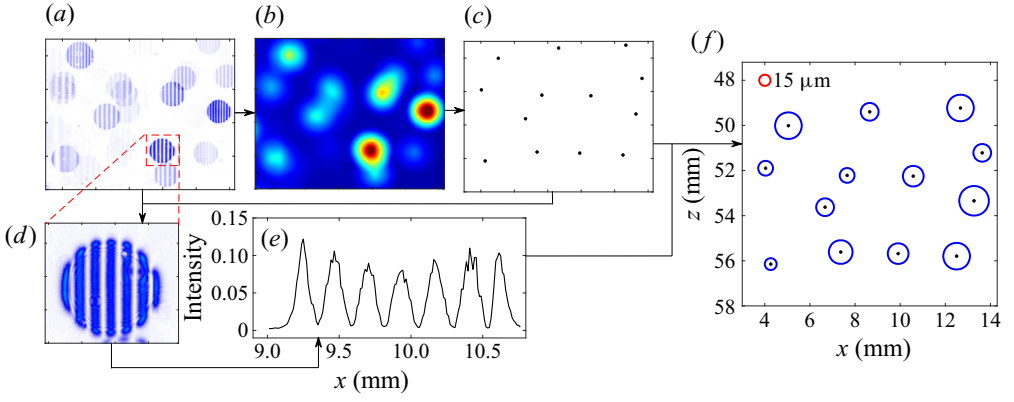

Figure 6. (*a*) Cropped view of a representative raw ILIDS image corresponding to the test condition with two perforated plates and mean bulk flow velocity of 14.0 m s^{-1}. (*b*) Convolution of the results in panel (*a*) using a disk-shaped mask. (*c*) Identified droplets centres. (*d*) Inset of panel (*a*), highlighting a sample fringe pattern. (*e*) Variation of the light intensity normal to the fringe pattern in panel (*d*). (*f*) Droplets centres and their corresponding diameters.

cells with area smaller than $0.5\bar{A}$ were labelled as clusters, and Voronoï cells with area larger than $2.2\bar{A}$ were labelled as voids. The identified clusters and voids corresponding to the Mie scattering image in figure 5(*a*) are shown by the blue and green colour cells in figure 5(*e*). As can be seen, clusters or voids may feature connected boundaries forming larger clusters and voids. Following Andrade *et al.* (2022), in the present study, the graph theory was used to identify and group the clusters/voids cells that are interconnected. For the results presented in figure 5(*e*), the identified clusters and voids are shown in figure 5(*f*). These clusters and voids were used for further analysis in § 4. It is important to note that the identified clusters and voids are formed due to both the interaction of the droplets with the background turbulent flow as well as (potentially) the air entrainment into the spray. Isolating the effect of the latter from that of the former on the clustering is not possible and was not performed in the present study.

3.2. *Droplets location and diameter estimation*

The ILIDS images were reduced to estimate the droplets location and diameters. A summary of the processes followed to reduce the ILIDS images is illustrated in figure 6. For clarity purposes, a cropped view of a representative raw ILIDS image is shown in figure 6(*a*), which corresponds to the test condition with two perforated plates and the mean bulk flow velocity of 14.0 m s^{-1}. Following the procedure used by Bocanegra Evans *et al.* (2015), the image shown in figure 6(*a*) was convoluted with a disk-shaped mask and the resultant image is shown in figure 6(*b*). The convoluted image features local maxima, which correspond to the centres of the droplets. The locations of the droplets centres were obtained, with the corresponding results shown by the black circular data points in figure 6(*c*). The variations of the light intensity along the lines that pass through the droplets centres and are normal to the corresponding fringe pattern were considered, with a sample fringe pattern and light intensity variation for one droplet shown in figure 6(*d*,*e*), respectively. Then, the fast Fourier transform of the light intensity variation corresponding to each droplet was obtained and the number of fringes was calculated. Finally, the droplet diameter was calculated using the number of fringe patterns and (2.1). Figure 6(*f*) presents the centres of the droplets as well as the blue circles, with their diameter relating to the

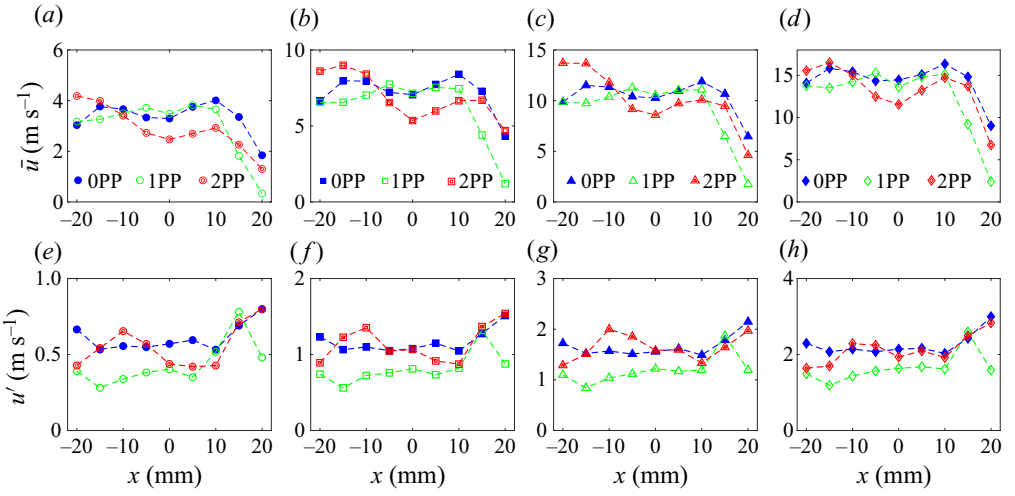

Figure 7. (*a–d*) Mean streamwise velocity for the mean bulk flow velocities of 3.5, 7.0, 10.5 and 14.0 m s^{-1}, respectively. (*e–h*) RMS streamwise velocity fluctuations for the mean bulk flow velocities of 3.5, 7.0, 10.5 and 14.0 m s^{-1}, respectively.

droplets' diameter. The diameters of the blue circles scale with the diameter of the red circle shown in the figure.

4. Results

The results are grouped into four subsections. In the first subsection, the characteristics of the background turbulent flow and the droplets diameter are discussed. In the second subsection, the degree of clustering is investigated. In the third subsection, the geometrical characteristics of the clusters and voids are presented. Finally, the joint characteristics of the clusters/voids and the droplets are presented in the last subsection.

4.1. *Background flow and droplet diameter characteristics*

The variations of the axial velocity mean ($\bar{u}$) and RMS fluctuations (u') along the x-axis are presented in the first and second rows of figure 7, respectively. The results in the first to fourth columns correspond to the mean bulk flow velocities of 3.5, 7.0, 10.5 and 14.0 m s^{-1}, and are shown using circular-, square-, triangular- and diamond-shaped data symbols, respectively. The blue, green and red colours pertain to zero, one and two perforated plates, respectively. The results presented in figure 7(*a–d*) feature a mean velocity deficit near $x = 0$, which is due to the wake of the spray injector, similar to the results presented by Petry *et al.* (2022). Also, the mean velocity profiles are nearly symmetric for the test conditions without a perforated plate; however, these profiles are nearly asymmetric for test conditions with one and two perforated plates, which are similar to those reported by Kheirkhah & Gülder (2015). Such asymmetry of the mean velocity profile is speculated to be caused by the relative positioning of the perforated plate with respect to the plane of the velocity measurements.

The results in figure 7(*e–h*) shows that for all tested mean bulk flow velocities and for the majority of the horizontal locations, the RMS of the streamwise velocity for one perforated plate is smaller than that for two perforated plates, which agrees with the results

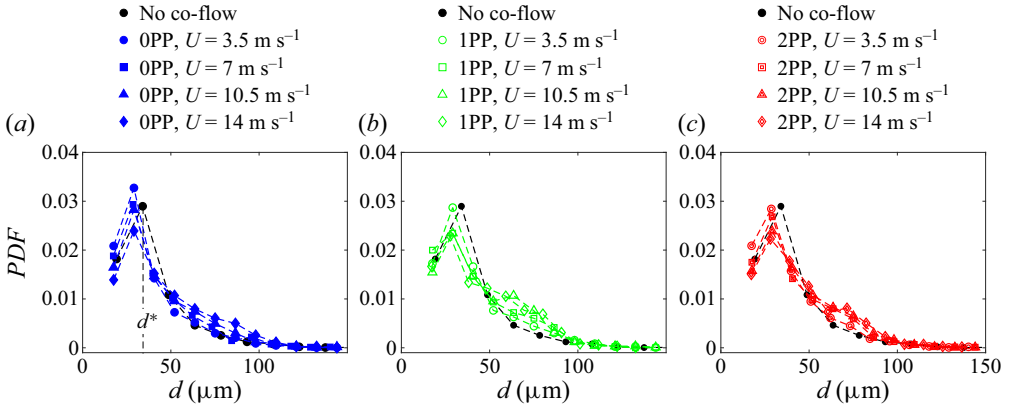

Figure 8. (*a–c*) PDFs of the droplet diameter for no perforated plate, one perforated plate and two perforated plates, respectively. The black circular data points are the PDF of the no co-flow test condition, which is repeated in panels (*a–c*) for comparison purposes.

of past investigations, see for example those of Kheirkhah & Gülder (2015). The results in figure 7(*e–h*) also show that the values of u' for no perforated plate are larger than those of one perforated plate and close to those of two perforated plates. It is speculated that the reason for the values of u' for no perforated plate being relatively large is due to the turbulence generated by the supporting bars of the tube holder shown in figure 2(*a*) and the wake of the spray injector. To assess this speculation, HWA experiments for a free jet (without the spray injector and without the tube holder) were performed (not presented as a test condition in table 1) and the values of u' were obtained. These were significantly smaller than those for the first turbulence generation mechanism. For example, for $U = 7.0\,\mathrm{m\,s^{-1}}$ and at $x = 0$, $u' = 0.34\,\mathrm{m\,s^{-1}}$ for a free jet without the spray injector and the tube holder; however, this parameter is $1.07\,\mathrm{m\,s^{-1}}$ with the injector and tube holder installed (i.e. the first turbulence generation mechanism). We speculate the reason for the values of u' being relatively smaller for the second turbulence generation mechanism (i.e. one perforated plate) than those for the first turbulence generation mechanism (zero perforated plate) is the break up of the eddies generated in the wake of the tube-holder bars by the perforated plate. The decrease of the RMS velocity fluctuations by the addition of the perforated plates has been reported by, for example, Wang *et al.* (2019).

The PDF of the droplet diameter for the first, second and third turbulence generation mechanisms are presented in figure 8(*a–c*), respectively. The PDFs were obtained considering all droplets within the field of view of the ILIDS measurements. For comparison purposes, the PDF of the droplet diameter for the no co-flow test condition is overlaid on figure 8(*a–c*) using the black circular data symbol. For the probability density function calculations, an 11.5 μm droplet diameter bin size was used, since this led to the best presentation of the results. For all test conditions, the mean ($\bar{d}$) and most probable droplet diameters were obtained and presented in figure 9(*a*,*b*), respectively. In figure 9(*a*,*b*), the error bars present twice the RMS of the droplet diameter fluctuations and the PDF bin size, respectively. The results in figure 9(*b*) show that the maximum change in the most probable droplet diameter as a result of changing the test condition is approximately $34 - 28 = 6\,\mu\mathrm{m}$. This is smaller than the bin size (11.5 μm) used for the PDF of the droplet diameter calculation. Thus, the results in figure 9(*b*) suggest that the most probable diameter of the droplets does not change noticeably by increasing the mean bulk flow velocity or changing the turbulence generation mechanism. This is

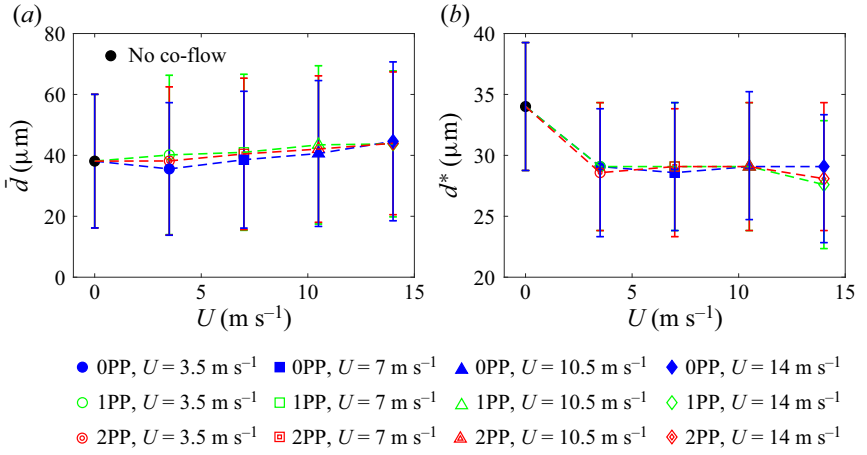

Figure 9. (*a*,*b*) Variations of the mean and most probable droplet diameter versus the mean bulk flow velocity for all test conditions.

speculated to be due to the measurement field of view being close to the injector, which strongly impacts the droplet diameter PDF. This finding is similar to that reported by Wang, Dalla Barba & Picano (2021). In fact, the study of Wang *et al.* (2021) showed that at relatively small vertical distances from the injector (less than 5 diameter of the nozzle) and for bulk flow Reynolds numbers comparable to those of the present study, changing this parameter does not influence the mean droplet diameter. The lack of sensitivity of the droplet diameter PDF to the test conditions, see figure 8, may have implications for the calculation of the Stokes number discussed earlier. Although the most probable droplet diameter is used for the estimation of the Stokes number, the PDFs of the droplet diameter do not change by changing the test condition. That is, alternative definitions of the Stokes number will yield similar trends in the present study, as a representative size for the droplet diameter will not change by varying the test conditions. Although the droplets diameter PDF estimated in the entire domain of investigation is not sensitive to the tested mean bulk flow velocity and the utilized turbulence generation mechanism, it is yet to be investigated how/if these parameters influence the PDF of the droplet diameter within the clusters and voids, which are studied in the following subsections.

4.2. *The droplets degree of clustering*

The Voronoï cells were used to study the droplets degree of clustering, following the procedure discussed in § 3. For all test conditions, the PDFs of the Voronoï cells area (A) are calculated and presented in figure 10(*a*). Also, the PDFs of the Voronoï cells area normalized by the locally averaged area ($A/\bar{A}$) are shown in figure 10(*b*) for all test conditions. As can be seen, the PDFs of $A/\bar{A}$ collapse for all test conditions, which is similar to the results presented by Obligado *et al.* (2014) and Monchaux *et al.* (2010). Overlaid on figure 10 is the PDF of the normalized area of the Voronoï cells provided these cells are spatially distributed following the RPP, with the formulation of PDF_{RPP} presented in (3.1). The results in figure 10 show that, for all test conditions, the PDFs of $A/\bar{A}$ intersect with PDF_{RPP} at $A/\bar{A} = 0.5$ and 2.2, which are shown by the vertical dashed lines in figure 10(*b*) and are similar to those shown in figure 5(*c*). Using the above normalized areas and following the procedure presented in § 3.1, the clusters and voids were identified, and the degree of clustering is studied below.

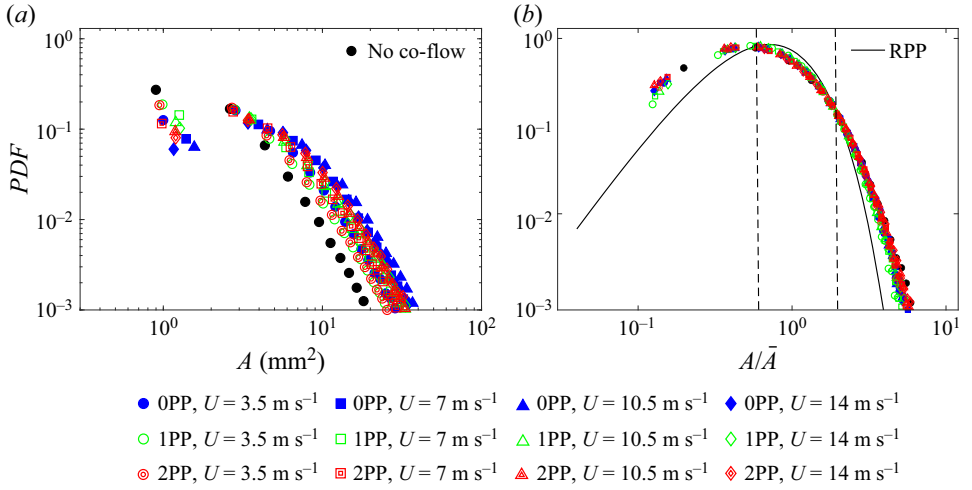

Figure 10. (*a*) PDFs of the Voronoï cells area, $PDF(A)$, for all test conditions. (*b*) PDF of the Voronoï cells area normalized by the locally averaged area. The solid black curve in panel (*b*) is the PDF of the normalized Voronoï cells area provided they were distributed following an RPP, with the formulation given in (3.1). The dashed lines in panel (*b*) correspond to $A/\bar{A} = 0.5$ and 2.2.

The degree of clustering, $(\sigma - \sigma_{RPP})/\sigma_{RPP}$, is presented in figure 11(*a*) for all test conditions. The results in the figure show that for test conditions with the co-flow, the degree of clustering is generally larger than that for the no co-flow test condition. Since the background turbulent flow characteristics do not necessarily vary monotonically with the number of perforated plates, best comparisons are obtained when the degree of clustering is presented versus St and Re_λ. The variations of the degree of clustering versus the Stokes number and the Taylor-length-scale-based Reynolds number are presented in figure 11(*b*,*c*), respectively. In addition to the results of the present study, those of Obligado *et al.* (2014), Monchaux *et al.* (2010), Sumbekova *et al.* (2017) and Petersen, Baker & Coletti (2019) are also overlaid on these figures. Analysis of the results presented by Monchaux *et al.* (2010) suggests that, for relatively small values of the Stokes number ($St \lesssim 10$) and for relatively small values of the Taylor-length-scale-based Reynolds number ($Re_\lambda \lesssim 200$), as St increases, the degree of clustering initially increases and reaches a maximum. Further increasing the Stokes number decreases the degree of clustering. For relatively small values of the Stokes number but relatively large values of the Taylor-length-scale-based Reynolds number ($Re_\lambda \gtrsim 200$), the degree of clustering is primarily influenced by Re_λ, see the results of Sumbekova *et al.* (2017). Specifically, increasing Re_λ increases the degree of clustering. Compared to past investigations, which correspond to particle-laden flows with relatively small Stokes numbers, for relatively large values of this parameter ($St \gtrsim 10$) and small values of the Taylor-length-scale-based Reynolds number, the degree of clustering is relatively small; and increasing St slightly increases the degree of clustering, plateauing at approximately 0.3. Acknowledging that the background turbulent flow of the present study may not be isotropic, which is different from the studies of Obligado *et al.* (2014), Monchaux *et al.* (2010), Sumbekova *et al.* (2017) and Petersen *et al.* (2019), further investigations are required to consider the influence of anisotropy of the background flow on the degree of clustering.

Wang *et al.* (2020) performed three-dimensional (3-D) direct numerical simulation (DNS) of particles clustering in homogeneous and isotropic turbulent flow in a box for

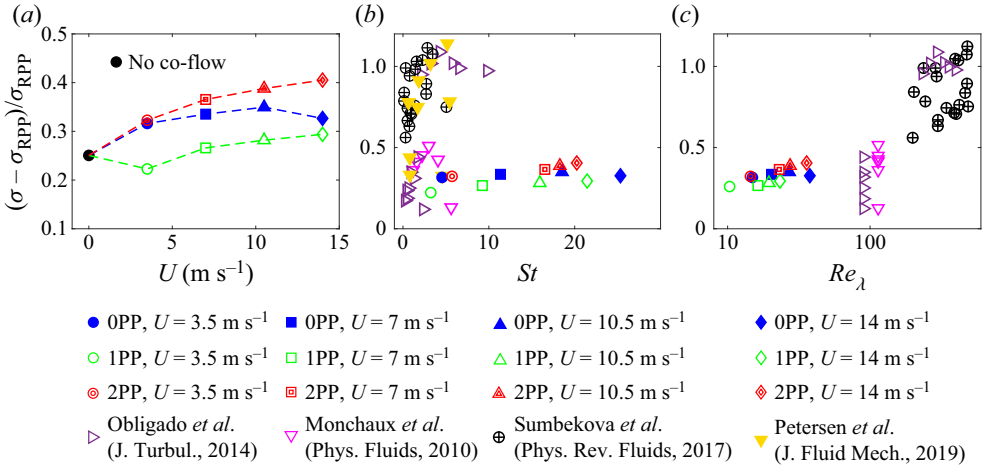

Figure 11. (*a–c*) Degree of clustering versus the mean bulk flow velocity, the Stokes number and Taylor-length-scale-based Reynolds number, respectively. Overlaid on panel (*b*,*c*) are the results of Obligado *et al.* (2014), Monchaux *et al.* (2010), Sumbekova *et al.* (2017) and Petersen *et al.* (2019).

Stokes numbers ranging from approximately 0 to 7. They estimated the standard deviation of the 3-D Voronoï cells volume. Results of Wang *et al.* (2020) show that the standard deviation of the 3-D Voronoï cells volume increases by increasing the Stokes number from approximately 0 to 1. However, further increase of the Stokes number to approximately 7 plateaus the standard deviation of the Voronoï cells volume. Although the analysis of Wang *et al.* (2020) is performed for the RMS of the Voronoï cells volume (which is different than the degree of clustering that pertains to the Voronoï cells area), the reported trend of Wang *et al.* (2020) follows that presented in figure 11(*b*) for matching Stokes numbers. Nevertheless, to our best knowledge, the plateau of the degree of clustering with increasing the Stokes number for $St \gtrsim 7$ is reported in the present study for the first time.

4.3. *The geometrical characteristics of clusters and voids*

Clustering of the clusters, length scales of the clusters and voids as well as how these are influenced by the non-dimensional parameters are discussed in the following subsections.

4.3.1. *Clustering of the clusters*

Although the analysis presented in § 4.2 allows for understanding the droplets degree of clustering, it does not provide insight into the clustering of the clusters, which is discussed in this subsection.

A representative spatial distribution of the clusters for the no co-flow test condition is presented in figure 12(*a*), see the blue regions in the figure. The centres of the area of the clusters were obtained and are shown by the black circular symbols in figure 12(*a*,*b*). The Voronoï cells associated with the centre of areas of the clusters were obtained and are shown in figure 12(*b*) using the blue lines. For all test conditions, the PDF of the Voronoï cells area obtained using the centre area of the clusters ($\tilde{A}$) divided by its mean value ($\overline{\tilde{A}}$) is presented in figure 13. Also overlaid on the figure is the PDF_{RPP}. Analysis similar to that performed for calculating the degree of clustering was employed to estimate the standard deviation of the area of the Voronoï cells formed by the clusters centre of area normalized

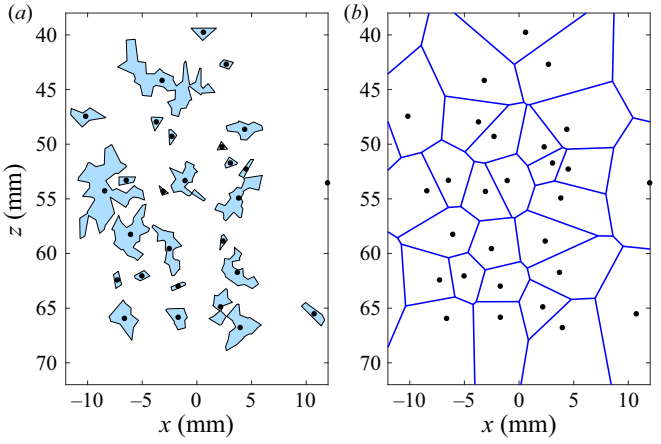

Figure 12. (*a*) Representative clusters. (*b*) The Voronoï cells formed by the clusters centre of area. In panel (*a*,*b*), the clusters centres of area are shown by the solid black data symbol. The results in panel (*a*,*b*) correspond to the no co-flow test condition.

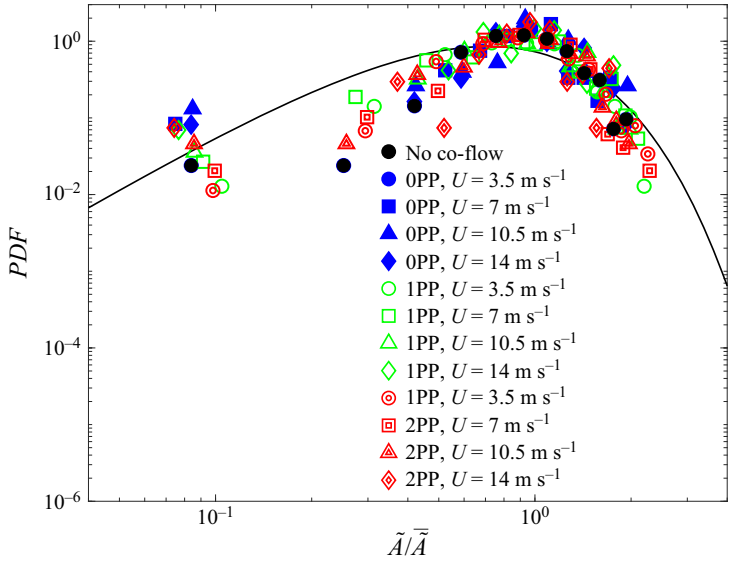

Figure 13. PDFs of the normalized Voronoï cells area formed by the clusters centre of area. The black solid curve is the PDF_{RPP}.

by their mean value. This was performed to asses the probability of the clustering of the clusters. For all test conditions, the standard deviation of $\tilde{A}/\overline{\tilde{A}}$ was calculated and it ranges from 0.3 to 0.4, which is smaller than $\sigma_{\mathrm{RPP}} = 0.53$. Monchaux *et al.* (2010) discussed that the standard deviations smaller than that of the RPP suggest that the clusters are distributed in an organized manner. As a result, the clustering of the clusters does not occur in the present study. Similar to the above analysis, Obligado, Cartellier & Bourgoin (2015) also investigated the clustering of the clusters. Their results show that the degree of clustering of the clusters was 0.8. Using the definition of the degree of clustering, the above means that the standard deviation of the area of the Voronoï cells formed by the

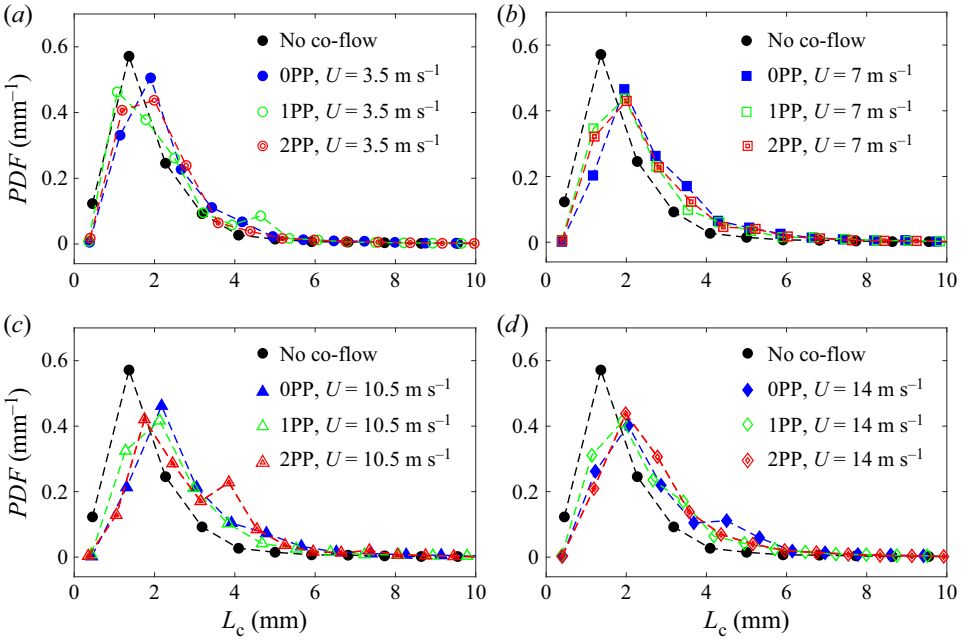

Figure 14. (*a–d*) PDFs of the cluster length scale for mean bulk flow velocities of $U = 3.5$, 7.0, 10.5 and 14.0 m s^{-1}, respectively. Overlaid by the black circular data symbol in panel (*a–d*) is the PDF of the cluster length scale for the no co-flow test condition.

clusters centre of area normalized by their mean value is $0.53 \times (0.8 + 1) \approx 1$ for the results of Obligado *et al.* (2015), which is significantly larger than those of the present study.

4.3.2. *Length scale of clusters and voids*

Following Petersen *et al.* (2019), the cluster and void length scales were defined as $L_c = \sqrt{A_c}$ and $L_v = \sqrt{A_v}$, respectively, with A_c and A_v being the cluster and void areas. The PDFs of L_c and L_v are presented in figures 14 and 15, respectively. The results in figures 14(*a–d*) and 15(*a–d*) correspond to mean bulk flow velocities of 3.5, 7.0, 10.5 and 14.0 m s^{-1}, respectively. For comparison purposes, the PDFs of the cluster and void length scales corresponding to the no co-flow test condition is presented by the solid black circular data symbol on the figures. The results in figures 14 and 15 show that for both clusters and voids, the presence of the co-flow generally leads to larger values of the most probable length scales.

Although the most probable cluster and void length scales are of importance, the majority of past investigations studied the relations between the mean values of the above length scales and the non-dimensional parameters, such as Taylor-length-scale-based Reynolds and Stokes numbers. The mean cluster and void length scales versus the mean bulk flow velocity are presented in figure 16(*a*,*b*), respectively. The error bars in the figures are twice the standard deviation of the corresponding data. For comparison purposes, the Taylor and integral length scales are also presented in figure 16(*c*,*d*), respectively. As can be seen, increasing the mean bulk flow velocity increases both the mean cluster and void length scales. The results show that cluster size is larger than the Taylor length scale but

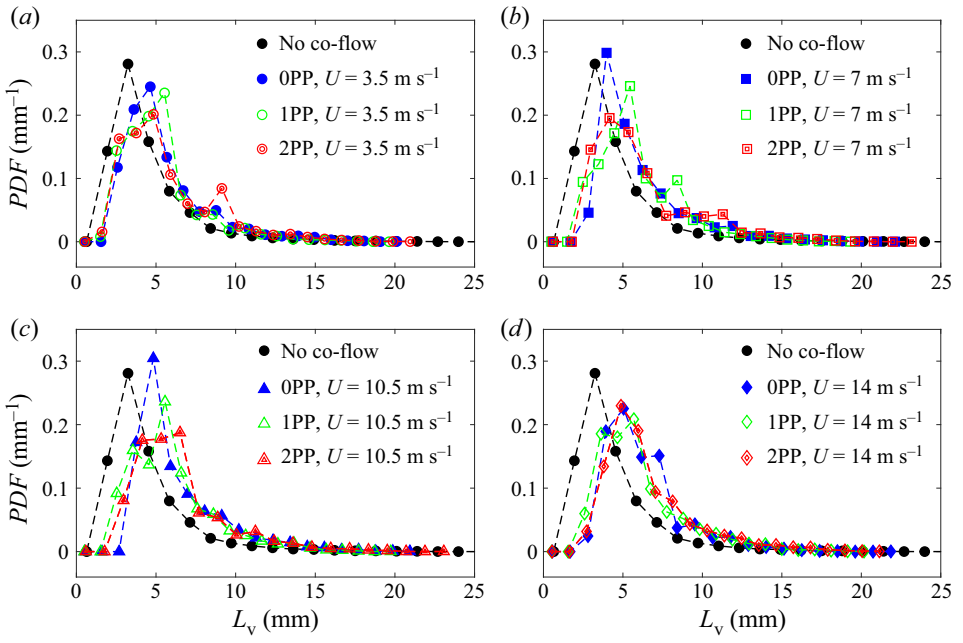

Figure 15. (*a–d*) PDFs of the void length scale for the mean bulk flow velocities of 3.5, 7.0, 10.5 and 14.0 m s^{-1}, respectively. The black circular data symbol is the PDF of the void length scale for the no co-flow test condition.

smaller than the integral length scale. The mean void length scale is, however, close to the integral length scale.

Variations of $\overline{L_c}$ normalized by the Kolmogorov length scale versus Re_λ is presented in figure 17(*a*). Also, overlaid on the figure are the results of Obligado *et al.* (2014) and Sumbekova *et al.* (2017), which are highlighted by the black dashed ellipse in the figure and correspond to relatively small Stokes numbers ($0 \lesssim St \lesssim 10$). The results of the present study are highlighted by the dashed red rectangle. As can be seen, the normalized cluster length scale of the present study and those of Obligado *et al.* (2014) and Sumbekova *et al.* (2017) do not follow a trend. Thus, variation of $\overline{L_c}/\eta$ versus the Stokes number were obtained and presented in figure 17(*b*). The results of Obligado *et al.* (2014) and Sumbekova *et al.* (2017) as well as Petersen *et al.* (2019) are overlaid on the figure for comparison. As can be seen, the normalized mean cluster length scale follows a trend when presented against the Stokes number. Specifically, it can be seen that increasing *St* almost linearly increases $\overline{L_c}/\eta$. Increasing the Stokes number to relatively large values leads to the response time of the droplets to become close to the time scale of large eddies. Thus, at large Stokes numbers, the droplets form relatively large clusters. This is consistent with the results presented by Petersen *et al.* (2019).

Variations of $\overline{L_v}/\Lambda$ versus Re_λ and *St* are presented in figure 17(*c*,*d*), respectively. Compared to the mean cluster length scale that can become approximately 100 times larger than the Kolmogorov length scale, the results in figure 17(*c*,*d*) show that the mean void length scale is of the order of the integral length scale. For large Stokes numbers, the droplets feature relatively large inertia, they interact with large scale eddies and, as a result, the droplets position at the periphery of the large scale eddies. This would suggest that for large Stokes numbers (such as those of the present study), the regions inside the

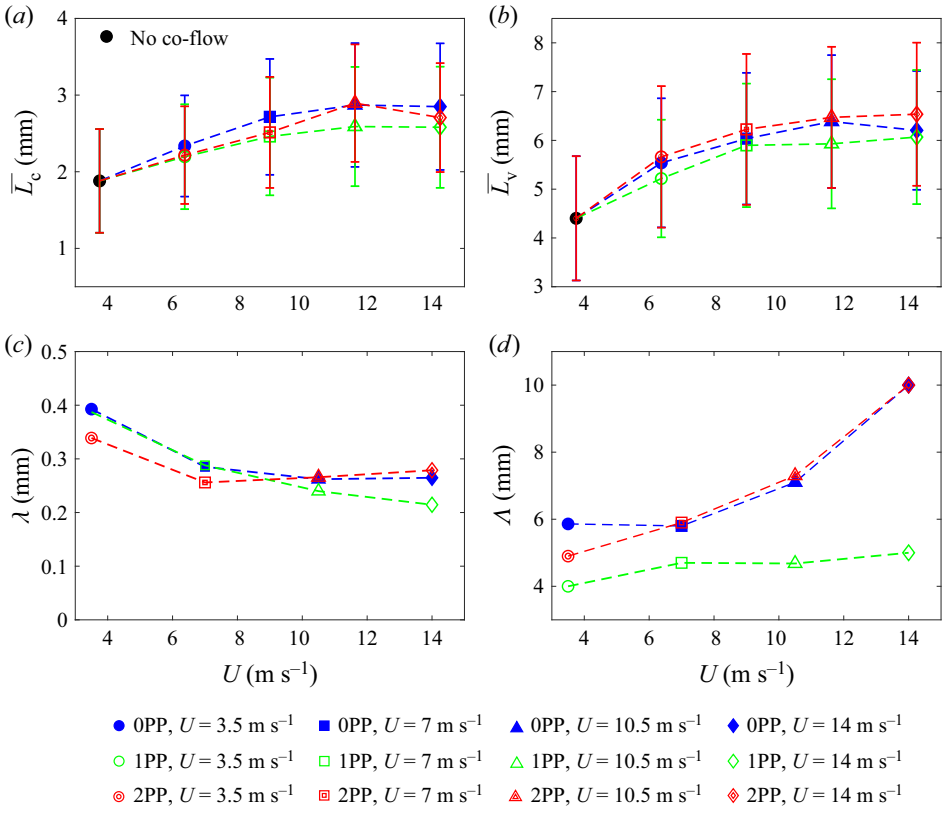

Figure 16. (*a*,*b*) Mean cluster and void length scales versus the mean bulk flow velocity, respectively. (*c*,*d*) Taylor and integral length scales versus the mean bulk flow velocity, respectively.

large eddies correspond to voids; and, as a result, these regions size is approximately the voids length scale, as shown in figure 17(*d*). Yoshimoto & Goto (2007) performed DNS of particles interacting with homogeneous and isotropic turbulence in a box, and they indeed showed that for $St = 10$, the length scale of voids saturate at the integral length scale of the turbulent flow. The results of the present study extends the findings of Yoshimoto & Goto (2007) from homogeneous and isotropic turbulence in a box to sprays in a turbulent co-flow with Stokes numbers up to 25.

4.4. *The inter-cluster and inter-void characteristics*

The results discussed in §§ 4.1–4.3 allow for understanding the characteristics of the droplets as well as those of clusters and voids individually; however, our understanding related to joint characteristics of the droplets and clusters/voids remains to be developed. In the following, the number density of the droplets inside the clusters and voids as well as the joint probability density function (JPDF) of the droplets diameter and clusters/voids areas are investigated.

4.4.1. *Number densities of droplets inside clusters and voids*

Figure 18 presents the JPDF of the number of droplets (N_P) inside the clusters and the area of the clusters. The contours are presented on a logarithmic scale (with a base of

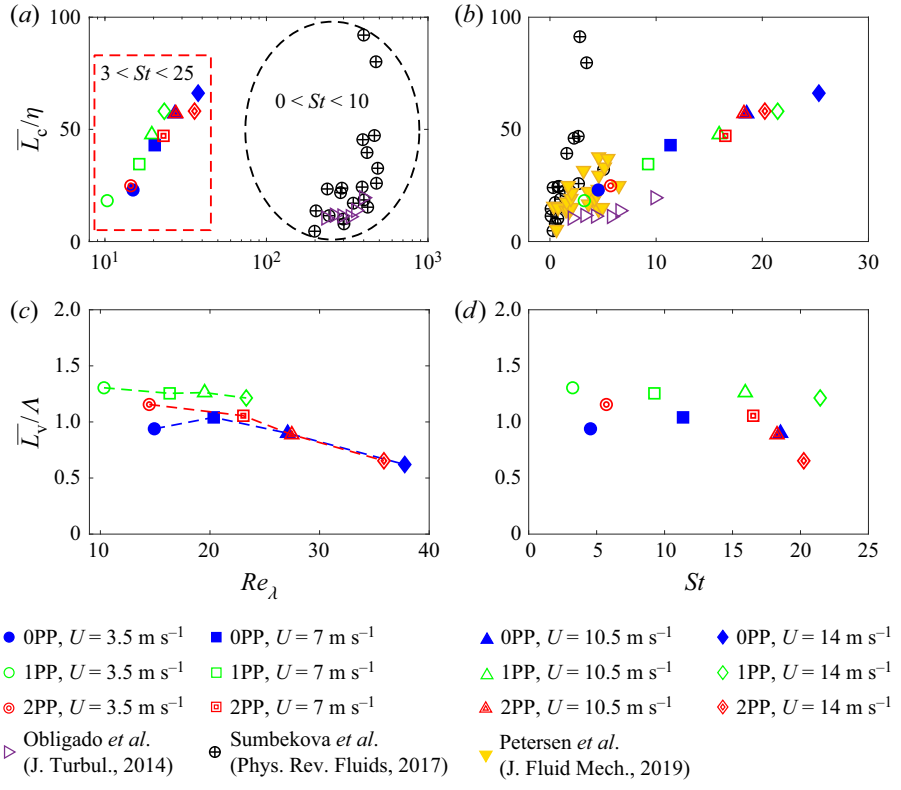

Figure 17. (*a*,*b*) Mean cluster length scale normalized by the Kolmogorov length scale versus Re_λ and St, respectively. Overlaid on panel (*a*,*b*) are the results of Obligado *et al.* (2014), Sumbekova *et al.* (2017) and Petersen *et al.* (2019). (*c*,*d*) Mean void length scale normalized by the integral length scale versus Re_λ and St, respectively.

10) for improving the clarity of presentation. The JPDFs in figure 18(*a*,*f*,*k*) correspond to the no co-flow test condition, are repeated and are presented for comparison purposes. The results in the second to fifth columns pertain to the mean bulk flow velocities of 3.5, 7.0, 10.5, and 14.0 m s^{-1}, respectively. The results in (*b–e*), (*g–j*) and (*l–o*) correspond to zero, one and two perforated plates, respectively. As can be seen, there exists a positive correlation between the number of particles and the area of the clusters, i.e. larger clusters contain more droplets. It can also be seen that increasing the mean bulk flow velocity decreases the slope of the relation between N_P and A_c, suggesting that the clusters dilute with increasing U. To quantify this, the combination of (N_P, A_c) data points at which the JPDF significantly changes by changing A_c at a fixed N_P were obtained, with representative results shown by the white circular data symbols in figure 18(*a*). The linear fits to these white data points were obtained, and the slopes of the lines were referred to as m_1 and m_2. Variations of m_1, m_2 and their average, $\bar{m} = 0.5(m_1 + m_2)$, versus the mean bulk flow velocity are shown in figure 19(*a–c*), respectively. These parameters quantify the number density of the droplets within the clusters. Similar to the above analysis, the JPDF of the number of droplets inside the voids and the area of the voids were obtained, with the corresponding results presented in figure 20. The figure indicators in figure 20 are identical to those in figure 18. Similar to the analysis presented for the results in figure 18(*a–c*), the slopes (m_1', m_2' and $\overline{m'} = 0.5(m_1' + m_2')$) for the results in figure 20 were extracted and

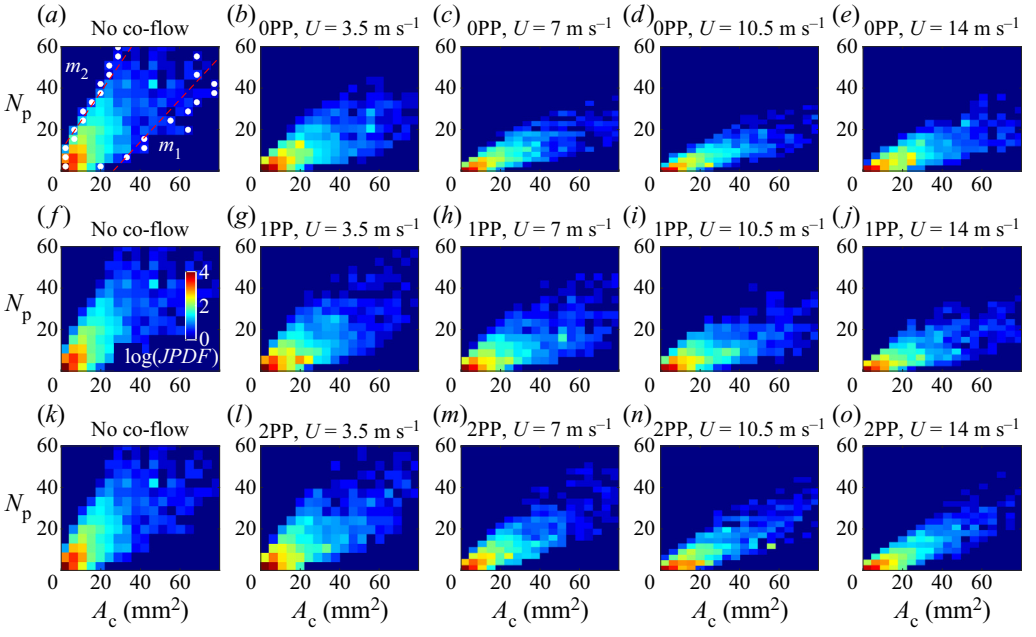

Figure 18. Logarithmic JPDF of the number of droplets within a given cluster area. Panel (*a*,*f*,*k*) corresponds to the no co-flow test condition and is repeated in each row for comparison purposes. The second to fifth columns correspond to the mean bulk flow velocities of 3.5, 7.0, 10.5 and 14.0 m s^{-1}, respectively. (*b–e*), (*g–j*) and (*l–o*) First to third turbulence generation mechanisms, respectively.

are shown in figure 19(*d–f*). Comparison of the results presented in figure 19(*a–c*) with those in figure 19(*d–f*) suggests that the number density of droplets within the clusters is generally one order of magnitude larger than that in the voids.

To investigate the effect of the non-dimensional parameters on the above number densities, the variations of $\bar{m}$ versus the Taylor-length-scale-based Reynolds and Stokes numbers are presented in figure 21(*a*,*b*), respectively. Also overlaid on the figures are the error bars, whose lengths correspond to $m_2 - m_1$. Similarly, the variations of $\overline{m'}$ versus the Taylor-length-scale-based Reynolds and Stokes numbers are also shown in figure 21(*c*,*d*), respectively, with the lengths of the error bars being $m_2' - m_1'$. The results suggest that for $St \gtrsim 10$, the number densities of the droplets inside the clusters and voids are nearly independent of the Stokes and the Taylor-length-scale-based Reynolds numbers and equal 0.45 and 0.06 mm^{-2}, respectively. However, for $St \lesssim 10$, increasing the Taylor-length-scale-based Reynolds number (which is accompanied by increase of the Stokes number) nearly decreases the number densities of the droplets in the clusters and voids.

On one hand, the results presented in figure 4 showed that increasing the Taylor-length-scale-based Reynolds and Stokes numbers both decrease the spray volume fraction. On the other hand, for $St \lesssim 10$, the results in figure 21 showed that increasing both Re_λ and St also decrease $\bar{m}$ and $\overline{m'}$. It is of interest to investigate the contributions of the decay of the number densities of the droplets inside the clusters and voids to the potential decay in the total number density of the droplets and if these contributions change by changing Re_λ and St. Figures 22(*a*) and 22(*b*) present the ratio of the total number of droplets detected in the Mie scattering field of view divided by the area of the field of view, M, versus the Taylor-length-scale-based Reynolds and Stokes numbers, respectively.

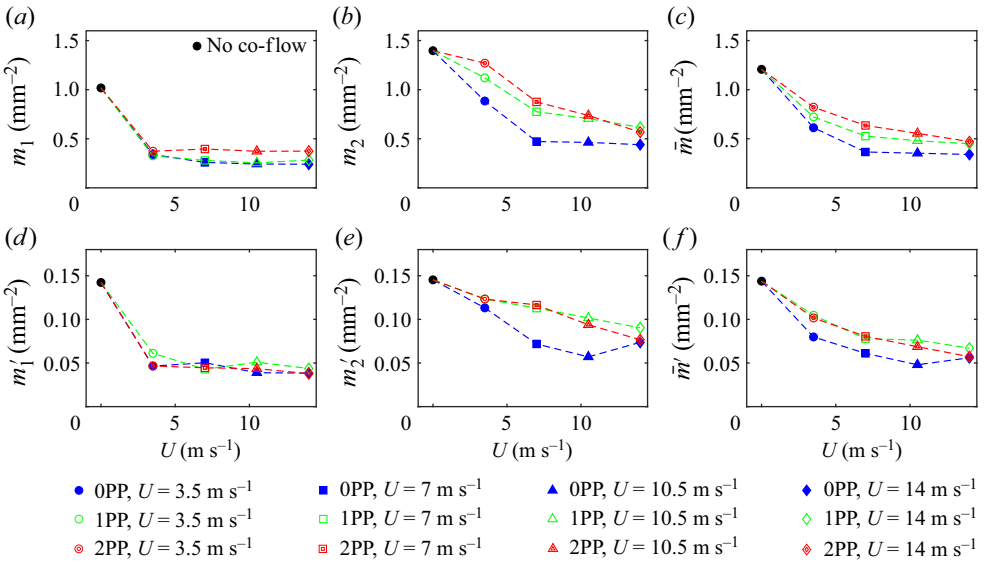

Figure 19. (*a–c*) Variations of m_1, m_2 and $0.5(m_1 + m_2)$ versus U, respectively. (*d–f*) Variations of m_1', m_2' and $0.5(m_1' + m_2')$ versus U, respectively.

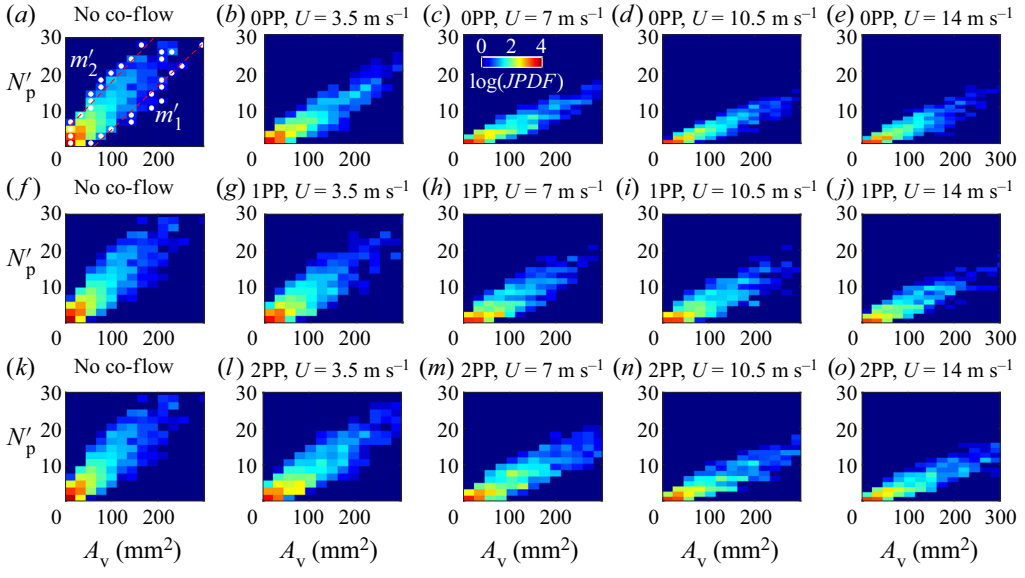

Figure 20. Logarithmic JPDF of the number of droplets and void area. Panel (*a*,*f*,*k*) corresponds to the no co-flow test condition and is repeated in each row for comparison purposes. The second to fifth columns correspond to the mean bulk flow velocities of 3.5, 7.0, 10.5 and 14.0 m s^{-1}, respectively. (*b–e*), (*g–j*) and (*l–o*) First to third turbulence generation mechanisms, respectively.

As can be seen, increasing these non-dimensional parameters decreases M, which is anticipated considering the decreasing trend in figure 4(c) and that the most probable droplet diameter is nearly unchanged by changing the test conditions. The variations of $\bar{m}/M$ versus Re_λ and St are presented in figure 22(*c*,*d*). Similarly, the variations of $\overline{m'}/M$

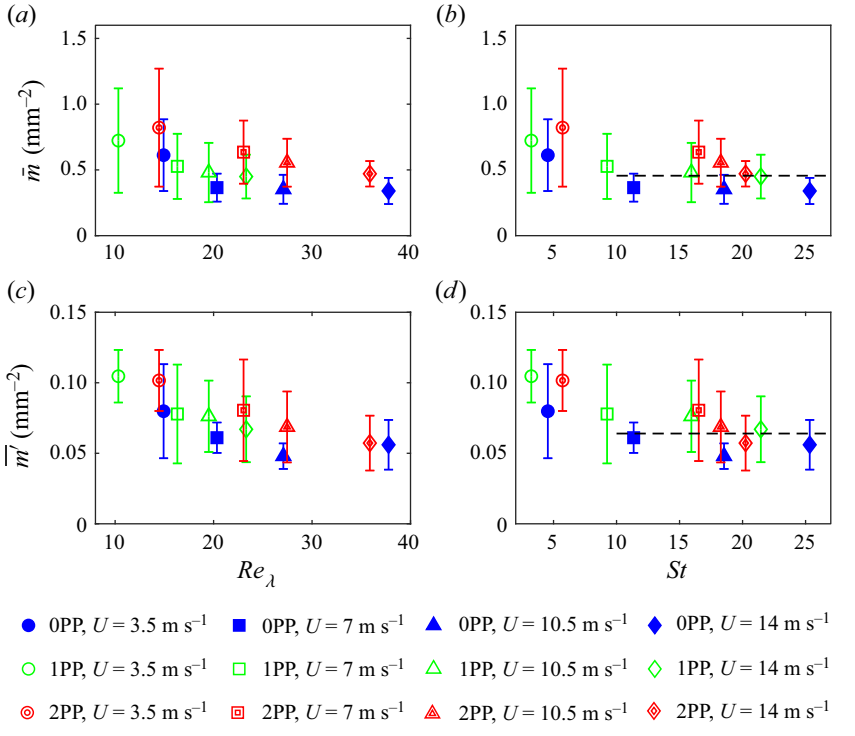

Figure 21. (*a*,*b*) Variations of $\bar{m}$ versus Re_λ and St, respectively. (*c*,*d*) Variations of $\overline{m'}$ versus Re_λ and St, respectively.

versus Re_λ and St are presented in figure 22(*e*,*f*), respectively. In figures 22(*c*,*d*) and 22(*e*,*f*), the lengths of the error bars are $m_2 - m_1$ and $m'_2 - m'_1$ normalized by the total droplets number density of the corresponding test condition. The results show that the number density of the droplets within the clusters and voids are 5.5 and 0.8 times the total number density, see the dashed lines in the figures, and these ratios do not change by changing the test conditions.

4.4.2. *Joint probability density function of droplet diameter and cluster/void area*

The JPDF of the clusters normalized area ($A_c/\overline{A_c}$) and the mean diameter ($\tilde{d}$) of the droplets within the clusters with normalized area of $A_c/\overline{A_c}$ is presented in figure 23. The bin size for the droplet diameter in the clusters was selected following the discussions presented in Appendix C. For presentation purposes, the JPDF contours are shown on a logarithmic scale with the base of 10. The results presented in figure 23(*a*,*f*,*k*) pertain to the no co-flow test condition, are identical and are shown for comparison purposes. The contours presented in the second to fifth columns correspond to the mean bulk flow velocities of 3.5, 7.0, 10.5 and 14.0 m s^{-1}, respectively. The results in figures 23(*b–e*), 23(*g–j*) and 23(*l–o*) pertain to test conditions with zero, one and two perforated plates, respectively. As can be seen, for all test conditions, the clusters with relatively small areas ($A_c/\overline{A_c} \lesssim 1$) are highly likely to exist. This is due to the PDF of the cluster length scale being skewed towards small values, as shown in figure 14. It can also be seen that near $\tilde{d} \approx 30\,\mu$m, which is close to the most probable droplet diameter measured in the ILIDS field of view and tabulated in table 1, the JPDFs feature significant values for a large range

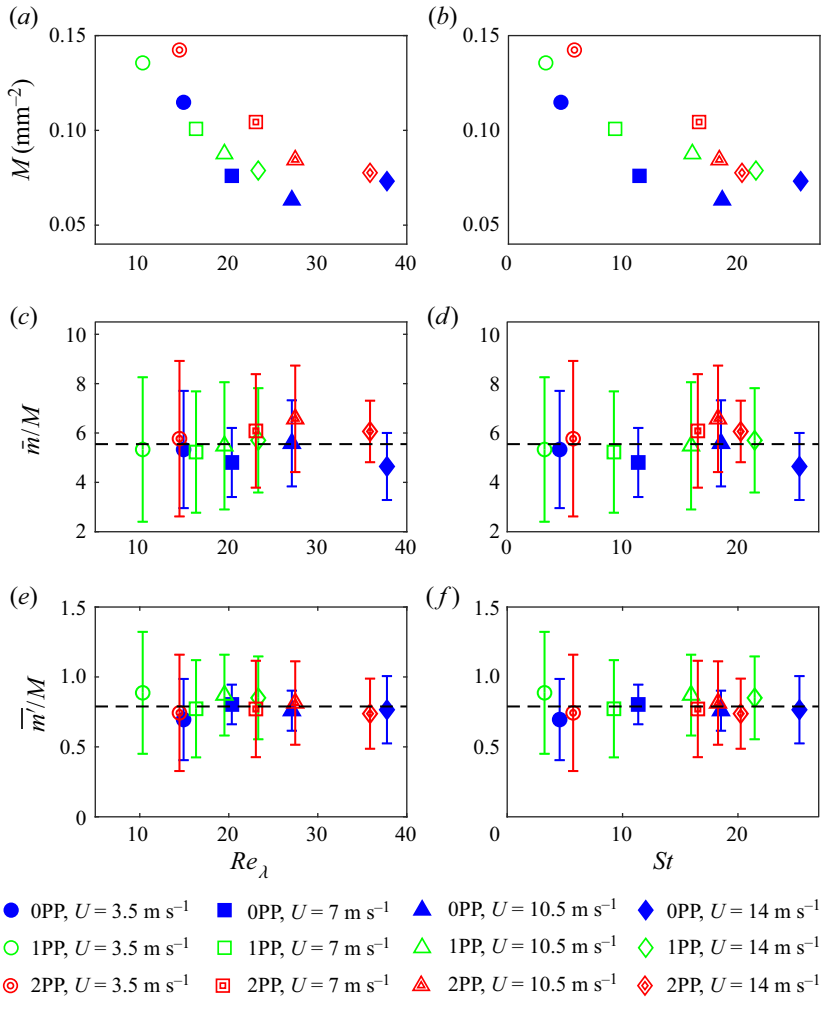

Figure 22. (*a*,*b*) Variations of the total number density versus Re_λ and St, respectively. (*c*,*d*) Variations of the number density of the droplets in the clusters divided by the total number density versus Re_λ and St, respectively. (*e*,*f*) Variations of the number density of droplets in the voids divided by the total number density versus Re_λ and St, respectively.

of cluster sizes. This means that for all test conditions, the majority of the clusters carry the droplets with the most probable diameter.

Comparison of the JPDFs for the no co-flow test condition (see panel *a*,*f*,*k*) with those that the co-flow provided shows that the probability of finding large droplets (mean diameter larger than approximately 100 μm) within a given normalized cluster area increases by adding the co-flow. This means that the presence of the co-flow facilitates the clustering of the large droplets. To quantify the effect of the co-flow on $\tilde{d}$, the contour of $JPDF(A_c/\overline{A_c}) = 10^{-3.5}$ was considered. Then, the intersections of this contour with a given normalized cluster area (here, $A_c/\overline{A_c} = 1$) were obtained, which are referred to as $\widetilde{d_1}$ and $\widetilde{d_2}$, see figure 23(*b*). The values of $\widetilde{d_1}$ and $\widetilde{d_2}$ change by varying the values of the selected *JPDF* as well as the selected $A_c/\overline{A_c}$; however, the trends of variation for $\widetilde{d_2} - \widetilde{d_1}$ with the governing parameters are independent of the selected *JPDF* value

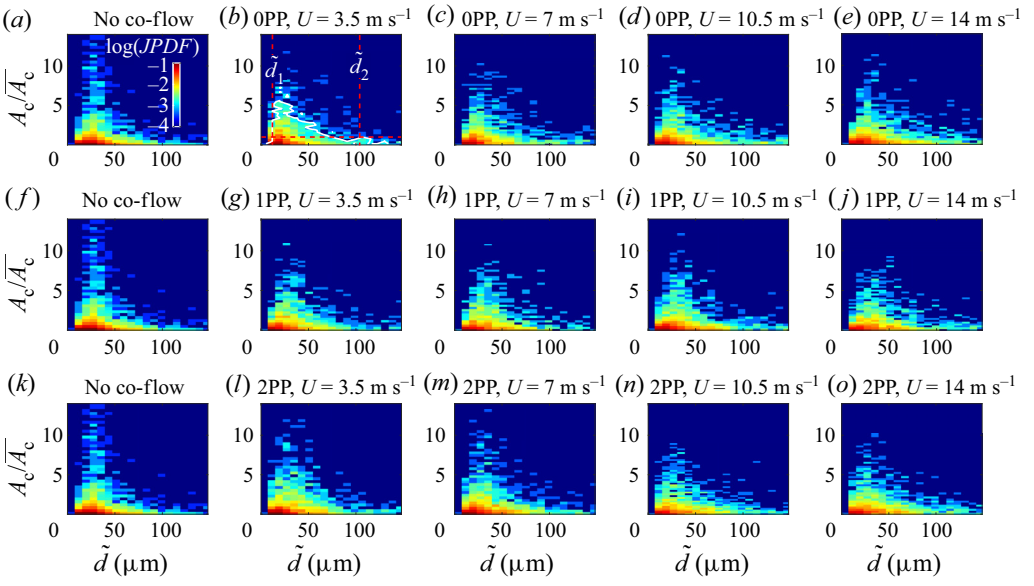

Figure 23. Logarithmic JPDF of the normalized clusters area ($A_c/\overline{A_c}$) and the mean diameter ($\tilde{d}$) of the droplets that exist within the cluster with normalized area of $A_c/\overline{A_c}$. Panel (a,f,k) corresponds to the no co-flow test condition and is repeated in each row for comparison purposes. The second to fifth columns correspond to the mean bulk flow velocities of 3.5, 7.0, 10.5 and 14.0 m s^{-1}, respectively. Panels (b–e), (g–j) and (l–o) present the results for the first to third turbulence generation mechanisms, respectively.

and $A_c/\overline{A_c}$. For all test conditions with the co-flow, the variations of $\widetilde{d_2} - \widetilde{d_1}$ versus Re_λ and St were obtained and presented in figure 24(a,b), respectively. The results show that increasing Re_λ and St generally increases $\widetilde{d_2} - \widetilde{d_1}$. As shown in figure 16($d$) and as tabulated in table 1, increasing the mean bulk flow velocity increases the integral length scale and decreases the Kolmogorov length scale. Thus, adding the co-flow (which is equivalent to increasing the Re_λ) increases the range of the turbulent eddy sizes. Following the mechanisms proposed by, for example, Goto & Vassilicos (2006), since turbulent eddies are responsible for the clustering of the droplets, the larger range of turbulent eddy sizes (see figure 16c,d) could increase the possibility of a broader range of droplet diameters to be positioned inside the clusters. As a result, a positive relation between $\widetilde{d_2} - \widetilde{d_1}$ and Re_λ as well as St is observed. This also suggests that the mechanism proposed by, for example, Goto & Vassilicos (2006) for droplets clustering may be extended to relatively large Stokes numbers of approximately 25, which was examined in the present study.

An analysis similar to the above was performed to investigate the joint characteristic of droplets and voids. Figure 25 presents the JPDF of the voids normalized area ($A_v/\overline{A_v}$) versus the mean diameter of droplets within the voids ($\widetilde{d'}$). The bin size for the droplet diameter in the voids was selected following the discussions in Appendix C. Similar to figure 23, the first to fifth columns correspond to the no co-flow, $U = 3.5$, 7.0, 10.5 and 14.0 m s^{-1} test conditions, respectively. Also, the results in the first to third rows pertain to the first to third turbulence generation mechanisms, respectively. The results presented in figure 25 show that the presence of the co-flow (compared with the no co-flow test condition) increases the probability of relatively large droplets to reside within the voids. The results in the second to fifth columns of figure 25 suggest that increasing

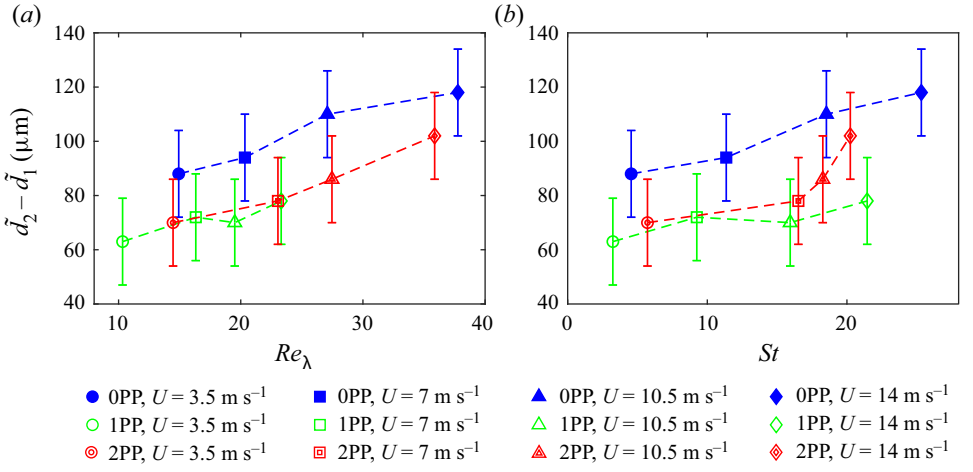

Figure 24. (*a*,*b*) Variations of $\tilde{d}_2 - \tilde{d}_1$ versus the Taylor-length-scale-based Reynolds and Stokes numbers, respectively.

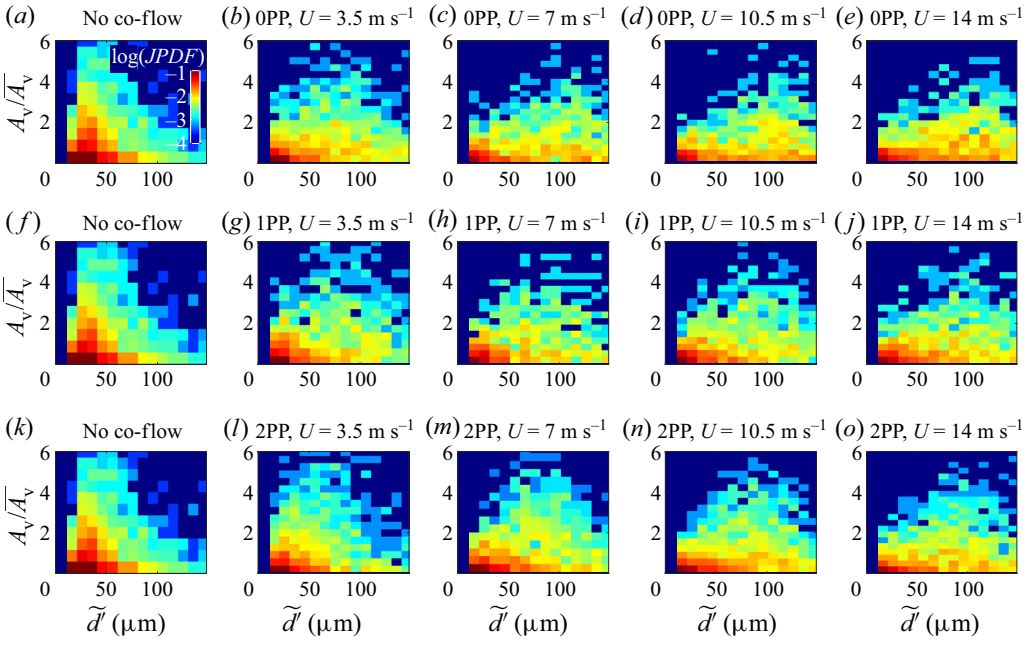

Figure 25. Logarithmic JPDF of the normalized area of the voids ($A_v/\overline{A_v}$) and the mean diameter of the droplets that exist within the voids ($\tilde{d}'$). Panel (*a*,*f*,*k*) corresponds to the no co-flow test condition and is repeated in each row for comparison purposes. The second to fifth columns correspond to the mean bulk flow velocities of 3.5, 7.0, 10.5 and 14.0 m s^{-1}, respectively. Panels (*b–e*), (*g–j*) and (*l–o*) present the results for the first to third turbulence generation mechanisms, respectively.

the mean bulk flow velocity and changing the turbulence generation mechanisms do not substantially change $JPDF(A_v/\overline{A_v}, \tilde{d}')$. This suggests that the turbulent co-flow may not facilitate positioning of the droplets within the voids.

5. Concluding remarks

Separate and joint characteristics of droplets diameter and clusters/voids size at relatively large Stokes numbers were investigated experimentally. Simultaneous Mie scattering and interferometric laser imaging for droplet sizing (ILIDS) were performed to acquire the spatial distribution of the droplets and their corresponding diameters. Also, separate hotwire anemometry was performed to characterize the background turbulent flow. A flow apparatus was used to produce a water spray injected in a turbulent co-flow of air. Mean bulk flow velocities of 0 (no co-flow), 3.5, 7.0, 10.5 and 14.0 $\mathrm{m\,s^{-1}}$ were examined. Three turbulence generation mechanisms (zero, one and two perforated plates) were used in the present study. The above mean bulk flow velocities and turbulence generation mechanisms allowed to vary the Kolmogorov-time-scale-based Stokes number and Taylor-length-scale-based Reynolds number from 3 to 25 as well as 10 to 38, which correspond to relatively large and small values (compared with those reported in the literature), respectively. The volume fraction of the spray was varied from approximately 10^{-6} to 2×10^{-6}, which rendered the tested sprays as dilute.

The Voronoï analysis was performed to calculate the degree of clustering as well as to identify the clusters and voids. The results showed that the addition of the co-flow to the spray generally increases the degree of clustering compared with the no co-flow condition. The results of the present study and those of past investigations were compiled and it was obtained that for relatively small values of the Stokes number ($St \lesssim 10$) and for relatively small values of the Taylor-length-scale-based Reynolds number ($Re_\lambda \lesssim 200$), as St increases, the degree of clustering initially increases and reaches a maxim value at $St \approx 2$–4. Further increasing the Stokes number decreases the degree of clustering. For relatively small values of the Stokes number but relatively large values of the Taylor-length-scale-based Reynolds number ($Re_\lambda \gtrsim 200$), the degree of clustering appears to be primarily influenced by Re_λ. Specifically, increasing Re_λ increases the degree of clustering. Compared with past investigations, which correspond to particle-laden flows with relatively small Stokes numbers, for relatively large values of this parameter ($St \gtrsim 10$) and small values of the Taylor-length-scale-based Reynolds number, the degree of clustering is relatively small; and increasing St slightly increases the degree of clustering, plateauing at approximately 0.3.

The clusters centre of area was obtained and the corresponding Voronoï cells were formed for all test conditions. The results showed that the standard deviation of these cells area normalized by their corresponding mean varies from 0.3 to 0.4 which is smaller than the standard deviation of a random Poisson process (i.e. 0.53). As a result, the clustering of the clusters does not occur for the conditions tested in the present study.

The length scales of the clusters and voids were estimated and compared with those of the background turbulent co-flow. The results showed that the mean void length scale was of the order of the integral length scale for all test conditions. However, the mean cluster length scale is smaller than the integral length scale but larger than the Taylor length scale. It was shown that increasing the Stokes number increases the mean cluster length scale to approximately 60 times the Kolmogorov length scale.

The results showed that the number density of the droplets within the clusters is approximately one order of magnitude larger than that for the voids, and both number densities decrease and then plateau with increasing the Stokes and Taylor-length-scale-based Reynolds numbers. It was obtained that the ratios of the clusters and voids number densities to the total number density of the spray are independent of the test conditions and nearly equal to 5.5 and 0.8, respectively. The joint probability

density function analysis was used to study the joint characteristics of the droplets and clusters/voids. It was concluded that a relatively wide range of cluster length scales can accommodate the most probable droplet diameter (approximately 30 μm) for all test conditions. It was shown that, although the joint PDF of the droplets diameter was not noticeably sensitive to the co-flow, increasing the Stokes and Taylor-length-scale-based Reynolds numbers increase the possibility of residing large droplets within the clusters. This was explained to be linked to increased range of eddy sizes interacting with droplets due to the increase of the above non-dimensional parameters. The present study provides insight into the number density of spray droplets within clusters and voids as well as the joint characteristics of the droplets and the cluster/voids area for relatively large Stokes numbers ($St \gtrsim 10$). This study also illustrates how the above characteristics are influenced by the variation of the Stokes and Taylor-length-scale-based Reynolds numbers.

Acknowledgments. The authors are grateful for the financial support from the University of British Columbia through the Eminence Fund program. S. Kheirkhah acknowledges the financial support from the Canada Foundation for Innovation.

Declaration of interests. The authors report no conflict of interest.

Author ORCIDs.
Ri Li https://orcid.org/0000-0003-4104-8134;
Sina Kheirkhah https://orcid.org/0000-0002-6195-1577.

Appendix A. Spray volume flow rate calibration

For the spray volume flow rate ($\dot{Q}$) calibration, first, the spray injector shown in figure 2 was connected to a sealed container; then, the upstream pressure of the injector (P_v) was set to several values ranging from approximately 50 to 800 kPa using the pressure controller shown as item (2) in figure 1. For each set value of the upstream pressure, a high-precision scale was used to measure the collected water mass, which was converted to volume by using the water density at the laboratory temperature of 20 °C. Then, the volume flow rate was calculated by dividing the volume of the collected water (in litres) to the time duration of the calibration experiment, which was 120 s. Figure 26 presents the variation of $\dot{Q}$ versus P_v. For all conditions tested in the present study, P_v was set to 206 kPa, which led to a spray volume flow rate of 22 cubic centimetres per minute (see the black circular data symbol in figure 26).

Appendix B. Procedure for registering the Mie scattering images to the ILIDS images and correcting the centre discrepancy

The centres of the droplets identified from the ILIDS images are not identical to those obtained from the Mie scattering images, and a discrepancy exists between the centres of the droplets identified from the above diagnostics. In addition to the present study, such discrepancy is also noted and discussed in the past investigations, see for example those of Boddapati *et al.* (2020) and Hardalupas *et al.* (2010). For the droplets and clusters/voids joint characteristics calculations, it is important to correct the discrepancy between the centres of the droplets obtained from the Mie scattering and ILIDS images. The procedure for correcting the above discrepancy and thus registering the Mie scattering to the ILIDS images is discussed in the following.

First, a 2-D target plate was manufactured and positioned in the location illuminated by the laser sheet in the experiments. Then, the images of the target plate were captured by the cameras used for collecting the Mie scattering and ILIDS images, with the

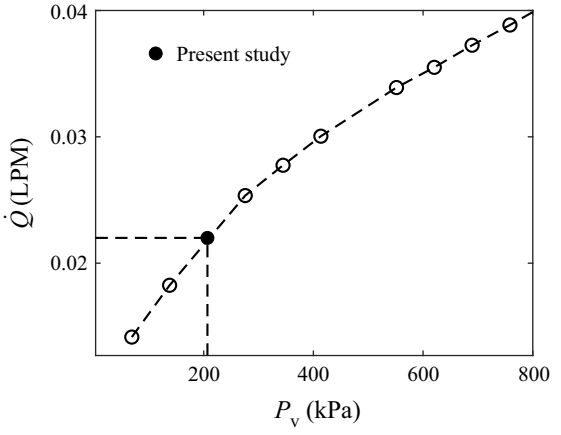

Figure 26. Relation between the water vessel pressure and the spray flow rate.

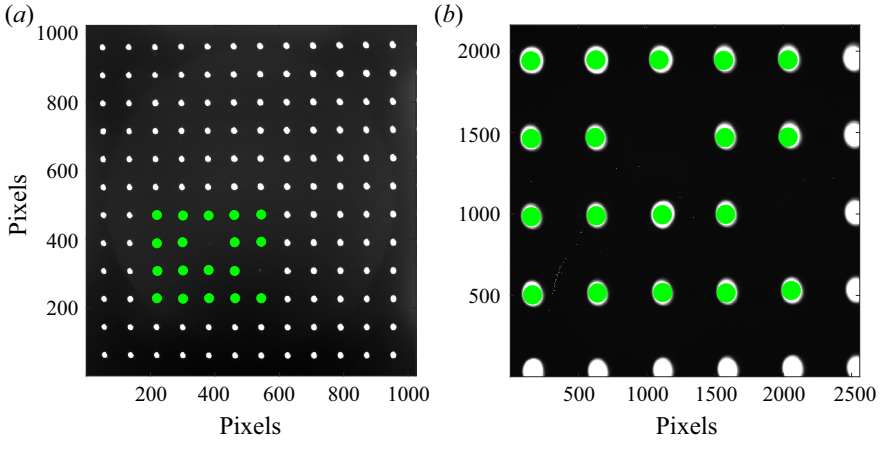

Figure 27. (*a*,*b*) Images of the target plate captured by the Mie scattering and ILIDS cameras, respectively.

collected images shown in figure 27(*a*,*b*), respectively. Eighteen points, see the green circles in figure 27(*a*), were considered and were identified in figure 27(*b*). The collective geometrical shape of these points was purposely selected to be asymmetric, facilitating the above identification. Then, the matrix that transforms data points in figure 27(*a*) to those in figure 27(*b*) was obtained. This transformation matrix was used for registering the Mie scattering images to the ILIDS images, with a representative result for such transformation discussed below.

Representative and simultaneously acquired Mie scattering and ILIDS images are shown in figure 28(*a*,*b*), respectively. The results correspond to the test condition with one perforated plate and the mean bulk flow velocity of $10.5\,\mathrm{m\,s^{-1}}$. Figure 28(*c*) presents the results in figure 28(*a*) after the application of the above transformation. Figure 28(*d*) shows that in figure 28(*b*) after application of the convolution discussed in § 3.2. The procedure discussed in § 3.2 was followed to identify the centres of the droplets from the results shown in figure 28(*d*), with the corresponding centres presented by the blue circular data points in figure 28(*e*). Overlaid on figure 28(*e*) are also the centres of the droplets obtained from binarizing the Mie scattering image in figure 28(*c*). The centres

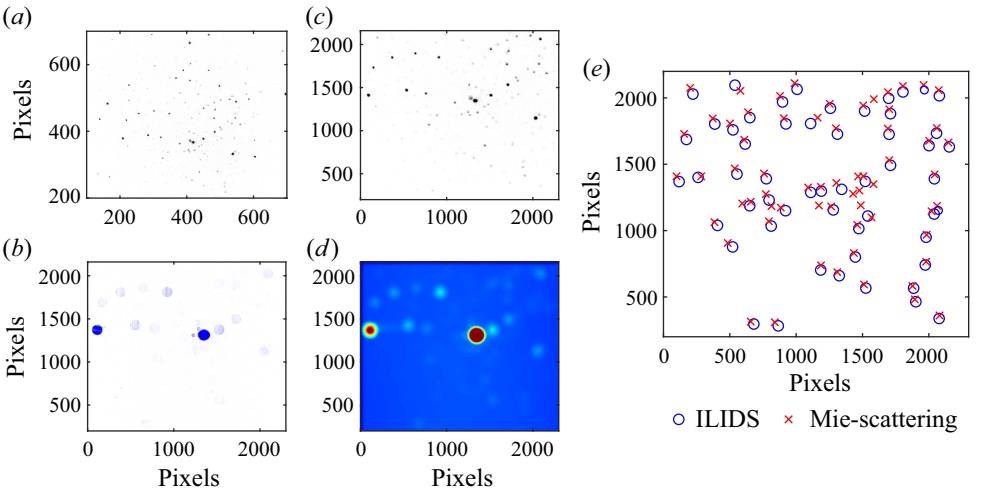

Figure 28. (*a*,*b*) Representative raw Mie scattering and ILIDS images, respectively. (*c*) Image obtained by mapping that shown in panel (*a*) to the imaging plane of the ILIDS camera. (*d*) Convolution of the results shown in panel (*b*) with a disk-shaped mask. (*e*) Centres of the droplets obtained from the ILIDS and Mie scattering images.

of the droplets obtained from the Mie scattering image are shown by the red cross data symbols in figure 28(*e*). As shown in this figure, a centre discrepancy exists even after the ILIDS image is registered to the Mie scattering image. The maximum centre discrepancy is approximately $59\,\text{pixels} \times 0.0114\,\text{mm}\,\text{pixel}^{-1} \approx 0.7\,\text{mm}$ in our experiments, which is similar to that (approximately 1 mm) reported by Hardalupas *et al.* (2010). In the study by Hardalupas *et al.* (2010), the centre discrepancy is independent of the droplet diameter but varies linearly along the imaging plane. Such variation is used by Hardalupas *et al.* (2010) to correct the location of the droplets. In the present study, however, a different approach was used to that of Hardalupas *et al.* (2010) to address the centre discrepancy. Since the spray used in the present study was dilute, the maximum centre discrepancy was relatively small and that the simultaneously acquired Mie scattering images allowed for understanding the true location of the droplets centres, a sorting algorithm in MATLAB was used to relate the droplets in the ILIDS image to the corresponding Mie scattering image. This relation was used to correct the discrepancy in the droplets locations.

Appendix C. Statistical error in calculation of the mean droplet diameter within clusters and voids

The number of the droplets detected from the ILIDS images is not equal to that obtained from the Mie scattering images. This can lead to statistical error in the calculation of the mean droplet diameter within the clusters and voids. To estimate this error, the PDF of the number of droplets detected within a cluster using the ILIDS and Mie scattering techniques were obtained for all test conditions and are presented in figure 29(*a*,*b*), respectively. As can be seen, the most probable number of droplets detected within a cluster using the ILIDS (n^*_{ILIDS}) and Mie scattering (n^*_{Mie}) techniques are 3 and 11, respectively. It is acknowledged that the difference between n^*_{ILIDS} and n^*_{Mie} is due to the limitation of the ILIDS technique. Specifically, the droplet diameter smaller than twice the diameter per fringe (which is $2 \times 1.97\,\mu\text{m} \approx 4\,\mu\text{m}$) and larger than the maximum resolvable diameter

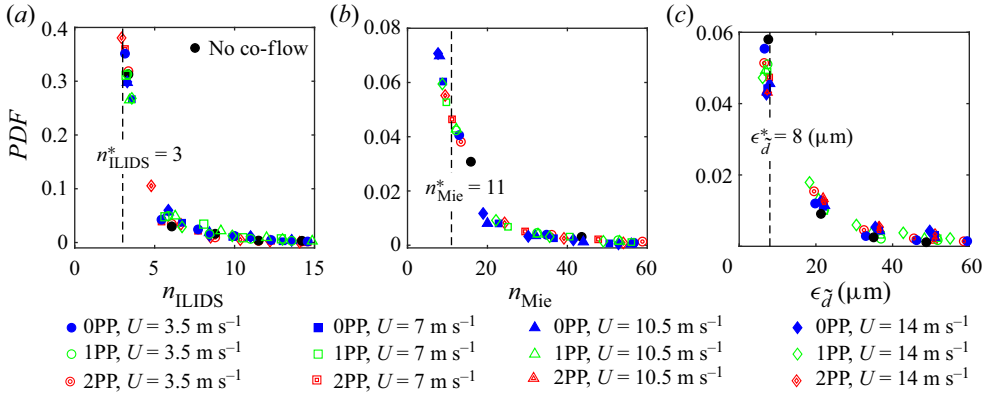

Figure 29. (*a*,*b*) PDF of the number of detected droplets within clusters using the ILIDS and Mie scattering techniques, respectively. (*c*) PDF of the statistical error in estimating the mean droplet diameter within a cluster.

(approximately 150 μm) cannot be calculated using ILIDS; however, a droplet with $d \lesssim 4$ and $d \gtrsim 150$ μm may be seen in the Mie scattering images. Also, the overlap between the droplets detected by the ILIDS does not allow for the calculation of the droplets diameter and leads to the elimination of such droplets in the diameter calculation, but the overlapping droplets in the ILIDS image could be seen in the Mie scattering image. The above are the systematic sources of error that relate to the limitations of the ILIDS and are not quantified in the present study. However, it is of interest to estimate the statistical uncertainty in calculating the mean diameter of the droplets within a cluster. To calculate this, first, the statistical error in estimation of the mean droplet diameter for a given cluster was obtained using (Moffat 1988)

$$\epsilon_{\tilde{d}} = \frac{\sigma_d}{\sqrt{n}}, \tag{C1}$$

where σ_d and n are the standard deviation of the droplet diameter within a cluster and n is the number of droplets within the cluster. For all test conditions, the PDF of $\epsilon_{\tilde{d}}$ was calculated and the results are shown in figure 29(*c*). As can be seen, the most probable value of $\epsilon_{\tilde{d}}$ is approximately 8 μm. Thus, the bin size for $\tilde{d}$ in the calculation of JPDF of the mean droplet diameter within a cluster and the normalized cluster area was selected to be 8 μm, which was reflected in the presentation of figure 23. An analysis similar to the above was performed to quantify the statistical error in estimating the mean droplet diameter within the voids, and the most probable value of the above error was 10 μm. This was used as the bin size of the mean droplet diameter in calculation of the JPDFs presented in figure 25.

References

Akamatsu, F., Miutani, Y., Katsuki, M., Tsushima, S. & Cho, Y.D. 1996 Measurement of the local group combustion number of droplet clusters in a premixed spray stream. *Proc. Combust. Inst.* **26** (1), 1723–1729.

Aliseda, A., Cartellier, A., Hainaux, F. & Lasheras, J.C. 2002 Effect of preferential concentration on the settling velocity of heavy particles in homogeneous isotropic turbulence. *J. Fluid Mech.* **468**, 77–105.

Andrade, P., Hardalupas, Y. & Charalampous, G. 2022 Study of preferential concentration in turbulent flows using combined graph theory and Voronoï analysis. *Phys. Fluids* **34** (5), 051704.

Baker, L., Frankel, A., Mani, A. & Coletti, F. 2017 Coherent clusters of inertial particles in homogeneous turbulence. *J. Fluid Mech.* **833**, 364–398.

BALACHANDAR, S. & EATON, J.K. 2010 Turbulent dispersed multiphase flow. *Annu. Rev. Fluid Mech.* **42**, 111–133.

BOCANEGRA EVANS, H., DAM, N., VAN DER VOORT, D., BERTENS, G. & VAN DE WATER, W. 2015 Measuring droplet size distributions from overlapping interferometric particle images. *Rev. Sci. Instrum.* **86** (2), 023709.

BODDAPATI, V., MANISH, M. & SAHU, S. 2020 A novel approach for conditional measurement of droplet size distribution within droplet clusters in sprays. *Exp. Fluids* **61**, 42.

BRANDT, L. & COLETTI, F. 2022 Particle-laden turbulence: progress and perspectives. *Annu. Rev. Fluid Mech.* **54**, 159–189.

CROWE, C.T., SCHWARZKOPF, J.D., SOMMERFELD, M. & TSUJI, Y. 2011 *Multiphase Flows with Droplets and Particles*. CRC.

ELGHOBASHI, S. 1994 On predicting particle-laden turbulent flows. *Appl. Sci. Res.* **52** (4), 309–329.

FERENC, J.-S. & NÉDA, Z. 2007 On the size distribution of Poisson Voronoi cells. *Physica* A **385** (2), 518–526.

FESSLER, J.R., KULICK, J.D. & EATON, J.K. 1994 Preferential concentration of heavy particles in a turbulent channel flow. *Phys. Fluids* **6** (11), 3742–3749.

FRANKEL, A., POURANSARI, H., COLETTI, F. & MANI, A. 2016 Settling of heated particles in homogeneous turbulence. *J. Fluid Mech.* **792**, 869–893.

GARCIA-MAGARINO, A., SOR, S., BARDERA, R. & MUNOZ-CAMPILLEJO, J. 2021 Interferometric laser imaging for droplet sizing method for long range measurements. *Measurement* **168**, 108418.

GOTO, S. & VASSILICOS, J.C. 2006 Self-similar clustering of inertial particles and zero-acceleration points in fully developed two-dimensional turbulence. *Phys. Fluids* **18** (11), 115103.

GOTO, S. & VASSILICOS, J.C. 2008 Sweep-stick mechanism of heavy particle clustering in fluid turbulence. *Phys. Rev. Lett.* **100** (5), 054503.

HARDALUPAS, Y., SAHU, S., TAYLOR, A.M.K.P. & ZAROGOULIDIS, K. 2010 Simultaneous planar measurement of droplet velocity and size with gas phase velocities in a spray by combined ILIDS and PIV techniques. *Exp. Fluids* **49** (2), 417–434.

HARDALUPAS, Y., TAYLOR, A.M.K.P. & WHITELAW, J.H. 1994 Mass flux, mass fraction and concentration of liquid fuel in a swirl-stabilized flame. *Intl J. Multiphase Flow* **20**, 233–259.

HASSAINI, R. & COLETTI, F. 2022 Scale-to-scale turbulence modification by small settling particles. *J. Fluid Mech.* **949**, A30.

HAYASHI, K., ICHIYANAGI, M. & HISHIDA, K. 2012 Measurements of droplets spatial distribution in spray by combining focus and defocus images. *Exp. Fluids* **49**, 417–434.

KHEIRKHAH, S. 2016 Experimental study of turbulent premixed combustion in V-shaped flames. PhD thesis, University of Toronto, Toronto, ON.

KHEIRKHAH, S. & GÜLDER, Ö.L. 2014 Topology and brush thickness of turbulent premixed V-shaped flames. *Flow Turbul. Combust.* **93** (3), 439–459.

KHEIRKHAH, S. & GÜLDER, Ö.L. 2015 Consumption speed and burning velocity in counter-gradient and gradient diffusion regimes of turbulent premixed combustion. *Combust. Flame* **162** (4), 1422–1439.

KUERTEN, J.G.M. 2016 Point-particle and LES of particle-laden turbulent flow-a state-of-the-art review. *Flow Turbul. Combust.* **97** (3), 689–713.

LEFEBVRE, A.H. & MCDONELL, V.G. 2017 *Atomization and Sprays*. CRC.

MAXEY, M.R. 1987 The gravitational settling of aerosol particles in homogeneous turbulence and random flow fields. *J. Fluid Mech.* **174**, 441–465.

MOFFAT, R.J. 1988 Describing the uncertainties in experimental results. *Exp. Therm. Fluid Sci.* **1** (1), 3–17.

MOHAMMADNEJAD, S., SACA, L. & KHEIRKHAH, S. 2022 A new compact active turbulence generator for premixed combustion: non-reacting flow characteristics. *Phys. Fluids* **34** (10), 105102.

MONCHAUX, R., BOURGOIN, M. & CARTELLIER, A. 2010 Preferential concentration of heavy particles: a Voronoï analysis. *Phys. Fluids* **22** (10), 103304.

MONCHAUX, R., BOURGOIN, M. & CARTELLIER, A. 2012 Analyzing preferential concentration and clustering of inertial particles in turbulence. *Intl J. Multiphase Flow* **40**, 1–18.

MORA, D., BOURGOIN, M., MININNI, P.D. & OBLIGADO, M. 2021 Clustering of vector nulls in homogeneous isotropic turbulence. *Phys. Rev. Fluids* **6** (2), 024609.

OBLIGADO, M., CARTELLIER, A. & BOURGOIN, M. 2015 Experimental detection of superclusters of water droplets in homogeneous isotropic turbulence. *Europhys. Lett.* **112** (5), 54004.

OBLIGADO, M., TEITELBAUM, T., CARTELLIER, A., MININNI, P. & BOURGOIN, M. 2014 Preferential concentration of heavy particles in turbulence. *J. Turbul.* **15** (5), 293–310.

PANDURANGAN, N. & SAHU, S. 2022 Spatial evolution of multi-scale droplet clusters in an evaporating spray. *Phys. Fluids* **34** (11), 113310.

PETERSEN, A.J., BAKER, L. & COLETTI, F. 2019 Experimental study of inertial particles clustering and settling in homogeneous turbulence. *J. Fluid Mech.* **864**, 925–970.

PETRY, N., SCHÄFER, D., LAMMEL, O. & HAMPP, F. 2022 Quantification of coflow effects on primary atomization of pressure swirl atomizers. *Intl J. Multiphase Flow* **149**, 103946.

POELMA, C. & OOMS, G. 2006 Particle-turbulence interaction in a homogeneous, isotropic turbulent suspension. *Appl. Mech. Rev.* **59** (2), 78–90.

QIENI, L., KAN, H., BAOZHEN, G. & XIANG, W. 2016 High-accuracy simultaneous measurement of particle size and location using interferometric out-of-focus imaging. *Opt. Express* **24** (15), 16530–16543.

READE, W.C. & COLLINS, L.R. 2000 Effect of preferential concentration on turbulent collision rates. *Phys. Fluids* **12** (10), 2530–2540.

SAHU, S. 2011 Experimental study of isothermal and evaporative sprays. PhD thesis, Imperial College London.

SAHU, S., HARDALUPAS, Y. & TAYLOR, A.M.K.P. 2016 Droplet–turbulence interaction in a confined polydispersed spray: effect of turbulence on droplet dispersion. *J. Fluid Mech.* **794**, 267–309.

SAHU, S., HARDALUPAS, Y. & TAYLOR, A.M.K.P. 2018 Interaction of droplet dispersion and evaporation in a polydispersed spray. *J. Fluid Mech.* **846**, 37–81.

SALAZAR, J.P.L.C., DE JONG, J., CAO, L., WOODWARD, S.H., MENG, H. & COLLINS, L.R. 2008 Experimental and numerical investigation of inertial particle clustering in isotropic turbulence. *J. Fluid Mech.* **600**, 245–256.

SAW, E.W., SHAW, R.A., AYYALASOMAYAJULA, S., CHUANG, P.Y. & GYLFASON, A. 2008 Inertial clustering of particles in high-Reynolds-number turbulence. *Phys. Rev. Lett.* **100** (21), 214501.

SQUIRES, K.D. & EATON, J.K. 1991 Preferential concentration of particles by turbulence. *Phys. Fluids* **3** (5), 1169–1178.

SUMBEKOVA, S., CARTELLIER, A., ALISEDA, A. & BOURGOIN, M. 2017 Preferential concentration of inertial sub-Kolmogorov particles: the roles of mass loading of particles, Stokes numbers, and Reynolds numbers. *Phys. Rev. Fluids* **2** (2), 024302.

TAGAWA, Y., MERCADO, J.M., PRAKASH, V.N., CALZAVARINI, E., SUN, C. & LOHSE, D. 2012 Three-dimensional Lagrangian Voronoïanalysis for clustering of particles and bubbles in turbulence. *J. Fluid Mech.* **693**, 201–215.

TAYLOR, G.I. 1938 The spectrum of turbulence. *Proc. R. Soc. Lond.* A **164** (919), 476–490.

THIMOTHÉE, R., CHAUVEAU, C., HALTER, F. & GÖKALP, I. 2016 Experimental investigation of the presence of fuel droplets after the passage of a flame front. In *27th European Conference on Liquid Atomization and Spray Systems, ILASS – Europe, Brighton, UK*. Available at: https://hal.science/hal-03556902.

VILLAFAÑE-ROCA, L., ESMAILY-MOGHADAM, M., BANKO, A. & EATON, J.K. 2016 A robust method for quantification of preferential concentration from finite number of particles. In *Center for Turbulence Research Annual Research Briefs*, pp. 123–135. Center for Turbulence Research.

WANG, J., DALLA BARBA, F. & PICANO, F. 2021 Direct numerical simulation of an evaporating turbulent diluted jet-spray at moderate reynolds number. *Intl J. Multiphase Flow* **137**, 103567.

WANG, J., YU, Q., ZHANG, W., ZHANG, M. & HUANG, Z. 2019 Development of a turbulence scale controllable burner and turbulent flame structure analysis. *Exp. Therm. Fluid Sci.* **109**, 109898.

WANG, L.-P. & MAXEY, M.R. 1993 Settling velocity and concentration distribution of heavy particles in homogeneous isotropic turbulence. *J. Fluid Mech.* **256**, 27–68.

WANG, X., WAN, M., YANG, Y., WANG, L.-P. & CHEN, S. 2020 Reynolds number dependence of heavy particles clustering in homogeneous isotropic turbulence. *Phys. Rev. Fluids* **5** (12), 124603.

WEISS, P., BHOPALAM, S.R., MEYER, D.W. & JENNY, P. 2021 On droplets that cluster and evaporate in reactive turbulence. *Phys. Fluids* **33** (3), 033322.

YOSHIMOTO, H. & GOTO, S. 2007 Self-similar clustering of inertial particles in homogeneous turbulence. *J. Fluid Mech.* **577**, 275–286.

ZHAO, R.-J., ZHAO, Y.-L., ZHANG, D.-S., LI, Y. & GENG, L.-L. 2021 Numerical investigation of the characteristics of erosion in a centrifugal pump for transporting dilute particle-laden flows. *J. Mar. Sci. Engng* **9** (9), 961.